



Originally published as:

Nilsson, A., Holme, R., Korte, M., Suttie, N., Hill, M. (2014): Reconstructing Holocene geomagnetic field variation: new methods, models and implications. - *Geophysical Journal International*, 198, 1, p. 229-248

DOI: <http://doi.org/10.1093/gji/ggu120>

Reconstructing Holocene geomagnetic field variation: new methods, models and implications

Andreas Nilsson,¹ Richard Holme,¹ Monika Korte,² Neil Suttie¹ and Mimi Hill¹

¹*Geomagnetism Laboratory, Department of Earth, Ocean and Ecological Sciences, University of Liverpool, Oliver Lodge Laboratories, Oxford Street, Liverpool L69 7ZE, UK. E-mail: andreas.nilsson@liv.ac.uk*

²*Helmholtz-Zentrum Potsdam, Deutsches GeoForschungsZentrum-GFZ, Stiftung des öff. Rechts Land Brandenburg, Telegrafenberg, D-14473 Potsdam, Germany*

Accepted 2014 March 27. Received 2014 March 24; in original form 2013 November 21

SUMMARY

Reconstructions of the Holocene geomagnetic field and how it varies on millennial timescales are important for understanding processes in the core but may also be used to study long-term solar-terrestrial relationships and as relative dating tools for geological and archaeological archives. Here, we present a new family of spherical harmonic geomagnetic field models spanning the past 9000 yr based on magnetic field directions and intensity stored in archaeological artefacts, igneous rocks and sediment records. A new modelling strategy introduces alternative data treatments with a focus on extracting more information from sedimentary data. To reduce the influence of a few individual records all sedimentary data are resampled in 50-yr bins, which also means that more weight is given to archaeomagnetic data during the inversion. The sedimentary declination data are treated as relative values and adjusted iteratively based on prior information. Finally, an alternative way of treating the sediment data chronologies has enabled us to both assess the likely range of age uncertainties, often up to and possibly exceeding 500 yr and adjust the timescale of each record based on comparisons with predictions from a preliminary model. As a result of the data adjustments, power has been shifted from quadrupole and octupole to higher degrees compared with previous Holocene geomagnetic field models. We find evidence for dominantly westward drift of northern high latitude high intensity flux patches at the core mantle boundary for the last 4000 yr. The new models also show intermittent occurrence of reversed flux at the edge of or inside the inner core tangent cylinder, possibly originating from the equator.

Key words: Archaeomagnetism; Palaeointensity; Palaeomagnetic secular variation.

1 INTRODUCTION

Global time-varying field models based on direct field measurements spanning the last few centuries (Bloxham *et al.* 1989; Bloxham & Jackson, 1992; Jackson *et al.* 2000) have greatly improved our understanding of the geomagnetic field and how it varies on decadal to centennial timescales, but do not provide a record of sufficient length to understand the physical processes that control the long-term changes in the geodynamo. Such models can be extended to millennial timescales using global compilations of palaeomagnetic field measurements obtained from archaeological artefacts, igneous rocks and lake or marine sediments (Korte *et al.* 2005; Genevey *et al.* 2008; Donadini *et al.* 2009). Over recent years major efforts have been made using these data compilations to reconstruct not only the dipole (Genevey *et al.* 2008; Knudsen *et al.* 2008; Valet *et al.* 2008; Nilsson *et al.* 2010) but also higher order structures of the field (Hongre *et al.* 1998; Constable *et al.* 2000; Korte & Constable 2003; Korte *et al.* 2011; Licht *et al.* 2013).

Such reconstructions can be used in a wide range of applications including investigations of westward and eastward motions in the core (Dumberry & Bloxham 2006; Dumberry & Finlay 2007; Wardinski & Korte 2008), the dynamics of high latitude flux patches (Korte & Holme 2010; Amit *et al.* 2011), field asymmetry related to archaeomagnetic jerks (Gallet *et al.* 2009) and lopsided inner core growth (Olson & Deguen 2012), geomagnetic field shielding of cosmic rays with implications for solar activity reconstructions (Muscheler *et al.* 2007; Snowball & Muscheler 2007; Lifton *et al.* 2008) and as relative dating tools for geological and archaeological archives (Lodge & Holme 2009; Pavón-Carrasco *et al.* 2009; Barletta *et al.* 2010).

Palaeomagnetic data are usually divided into two groups: (i) archaeomagnetic data (here taken to include lavas) containing spot readings in time of both direction and intensity and (ii) sedimentary records constituting continuous depositional sequences of directions and relative intensities. Data from the latter group are generally considered less reliable but provide a better spatial and

temporal (ST) geographical distribution, which is essential for global field modelling. Comparisons between dipole moment and dipole tilt reconstructions with more comprehensive spherical harmonic models highlight potential problems with recovering even the most basic (i.e. dipole) component of the field (Knudsen *et al.* 2008; Valet *et al.* 2008; Nilsson *et al.* 2010). One of the main reasons for these differences stems from the use and treatment of sedimentary data to constrain the models. Several studies have noted inconsistencies within the current sedimentary database (Donadini *et al.* 2009), which are mainly due to dating uncertainties (Korte *et al.* 2009; Nilsson *et al.* 2010; Korte & Constable 2011; Licht *et al.* 2013), sometimes on the order of thousands of years (Doner 2003; Nourgaliev *et al.* 2005). In addition to uncertainties related to dating, the magnetic signal may also be both offset in time and inherently smoothed because of the gradual, but largely unknown, process by which the magnetization is locked in to the sediments (see Roberts & Winklhofer 2004). Sedimentary records can also contain systematic errors in both declination and inclination due to problems with orienting the retrieved sediment cores (e.g. Constable & McElhinny 1985; Ali *et al.* 1999; Snowball & Sandgren 2004; Stoner *et al.* 2007) but also due to different problems related to sedimentary processes, such as compaction, which may lead to shallow inclinations (Blow & Hamilton 1978; Anson & Kodama 1987; Tauxe, 2005). A lack of consistent data treatment and/or data availability makes it difficult to estimate these data uncertainties (Panovska *et al.* 2012).

In this study, we present three new palaeomagnetic field models spanning the last 9000 yr (pfm9k), building on the recent work of Korte *et al.* (2011). One of the main purposes of this study is to address the issues with the sedimentary records mentioned above in order to extract more information from this data set. We do this by introducing new data treatments including redistributions of weight given to the different data sources and types during the inversion and new adjustments/calibrations of relative data based on preliminary field estimates. The results are evaluated by comparisons with other models for the same time period and models based on synthetic data sets derived from the historical field model *gufm1* (Jackson *et al.* 2000).

2 DATA

2.1 Initial data set

The palaeomagnetic data used to develop the new models were based on a similar initial data set used to construct CALS10k.1b (Korte *et al.* 2011). This data set consists of archaeomagnetic declination, inclination and intensity data obtained from the online GEOMAGIA50 database (Donadini *et al.* 2006; Korhonen *et al.* 2008) 2013 August 22, and sedimentary palaeomagnetic declination, inclination and relative palaeointensity records from the SED12k data compilation (Donadini *et al.* 2009; Korte *et al.* 2011).

Prior to making any adjustments, the following data, regarded as unsuitable for the modelling procedure, were rejected or replaced based on information in the original publications or comparisons with other data: (i) two lake sediment records, Vatndalsvatn (Thompson & Turner 1985) and Lakes Naroch and Svir (Nourgaliev *et al.* 2005) that were dated using bulk sediment radiocarbon dates that produce suspiciously old ages, were removed. It is a known problem that radiocarbon dating of bulk sediments can produce too old ages due to the incorporation of ‘old’ carbon from the bedrock or soil ‘diluting’ the contemporary ^{14}C in the sediments (see, e.g. Björck & Wohlfarth 2001). In the case of Vatndalsvatn, for exam-

ple, the offset between calibrated ^{14}C age and true age produced by this effect has been estimated to c. 1200 yr using a combination of lead isotopes, caesium and radiocarbon analyses (Doner 2003). (ii) Likewise all archaeomagnetic data with large dating uncertainties ($\sigma_{\text{age}} > 500$ yr) were also removed. (iii) Two relative palaeointensity records (AAM, WPA—see Table 1 for full names) and one declination record (VIC) were removed based on incompatible long-term trends over the Holocene. If included, most of the data from these records would be removed as outliers anyway during the model rejection analyses (see Section 3.1). (iv) Finally, the relative palaeointensity data from four Scandinavian lake records (FUR, FRG, MOT and SAR), which had been standardized for construction of a Fennoscandian master curve FENNORPIS (Snowball *et al.* 2007), were replaced with the originally published data (Ian Snowball, 2012, personal communication).

2.2 Resampling the sedimentary data

The SED12k data compilation consists of a mix of data from single core studies represented by individual measurements to smoothed data stacks based on multiple measurements from several parallel cores. In addition, the measurements are either performed on discrete samples, collected every 2–3 cm, or on 1–2 m long u-channels samples. The latter usually results in more data points, often with a 1-cm resolution, but each measurement represents an average over a depth range of 15–20 cm depending on the size of the sense-coil and the shape of the pick-up function (Weeks *et al.* 1993). The heterogeneous nature of the data set leads to an inappropriate weighting of the data during the modelling. For example, a u-channel record from a single core (WPA), which consists of correlated measurements, is represented by more than six times as many data points than another arguably more reliable record (BIW) from the same region, based on measurements from three parallel cores, where only the smoothed data are available. To avoid such problems we binned all sedimentary records in 50-yr bins giving equal weight to each site at any given time. This approach reduces the number of sedimentary data by more than 70 per cent (from 67 802 to 19 865), which effectively adds weight to archaeomagnetic data.

2.3 Prior dipole field model

To rescale/adjust the sedimentary palaeomagnetic data and to assign intensity uncertainties we use a prior dipole field model. This model was constructed by combining a dipole tilt reconstruction, DE_{FNBKE} (Nilsson *et al.* 2011), based on selected sedimentary data, with a dipole moment estimate based on cosmogenic radionuclides. Cosmogenic radionuclides (e.g. ^{10}Be , ^{14}C) are produced in the atmosphere by interactions with cosmic rays at a rate which is inversely related to the strength of the geomagnetic field (Lal & Peters 1967). To estimate variations in the dipole moment we used ^{10}Be flux data from the GRIP ice core (Muscheler *et al.* 2004; Vonmoos *et al.* 2006), which were first low-pass filtered with a cut-off frequency of $1/3000 \text{ yr}^{-1}$ to remove solar activity induced production variations (Muscheler *et al.* 2005). The ^{10}Be flux data were then converted to dipole moment using the transfer function from Lal (1988) and normalized by minimizing the resulting dipole field model misfit to all available archaeointensity data (ignoring data uncertainty estimates) over the model time period. The dipole component from *gufm1* was added to extend the model to the present, resulting in a gap between 1350 and 1590 AD that was bridged by linear interpolation. See Section 4.2 (Fig. 6) for comparisons between the prior dipole field model and other geomagnetic field models.

Table 1. Summary of the sediment records used in this study.

Abb.	Location	Sample type	N_{bin}^a	α_{63}^b (°)	σ_{F}^b (μT)	ΔD_{MOD}^c (°)	ΔD_{ARC}^c (°)	ΔT_{AVG}^d (yr)	ΔT_{MAX}^d (yr)	Ref. ^e
AAM	Alaskan margin, Arctic Sea	U-channel	112	3.5	–	14.7	–	108	400	1
AD1	Adriatic Sea, Italy	U-channel	122	3.5	6.2	–	–	–113	450	2
AD2	Adriatic Sea, Italy	U-channel	79	3.5	6.5	–	–	192	500	2
ANN	Lac d'Annecy, France	Discrete	43	3.4	–	3.0	(0.1)	–42	305	3
ARA	Lake Aral, Kazhakstan	Smoothed	25	3.5	–	14.7	(16.2)	–259	400	4
ASL	Lake Aslikul, Russia	Smoothed	72	3.5	–	9.5	(11.1)	360	500	5
BAI	Lake Baikal, Siberia, Russia	Smoothed	61	3.5	6.7	(–6.6)	–2.7	283	500	6
BAM	Lake Barombi Mbo, Cameroon	Smoothed	131	3.5	–	–3.5	–	–55	300	7
BAR	Lake Barrine, North Queensland, Australia	Discrete	169	6.7	4.9	34.4	(46.5)	26	200	8,9
BEA	Beaufort sea, Arctic Ocean	U-channel	84	3.5	8.9	–28.2	(–33.3)	–4	300	10
BEG	Lake Begoritis, Greece	Discrete	106	2.5	–	–1.5	(0.7)	35	250	11
BIR	Birkat Ram, Israel	Discrete	106	4.1	6.1	(–2.0)	–0.9	–181	450	12,13
BIW	Lake Biwa, Japan	Smoothed	185	3.5	–	8.1	(9.0)	33	400	14
BI2	Lake Biwa, Japan	Smoothed	108	3.5	6.3	8.8	(11.8)	37	500	15
BLM	Lake Bullenmerri, Western Victoria, Australia	Smoothed	83	3.5	–	–3.1	(3.1)	27	195	16
BOU	Lac du Bourget, France	Discrete	35	3.2	–	–1.9	(0.5)	90	150	3
CAM	Brazo Campanario, Argentina	Smoothed	137	3.5	–	0.6	–	–77	300	17
CHU	Chukchi Sea, Arctic Ocean	U-channel	155	3.5	7.5	–3.8	–	–34	250	10
DES	Dead Sea, Israel	Discrete	133	3.7	–	–1.4	(–1.4)	–150	500	18
EAC	Lake Eacham, North Queensland, Australia	Discrete	106	7.5	6.5	13.7	(9.1)	–10	150	8,9
EIF	Eifel maars, Germany	Smoothed	185	3.1	–	–0.2	(2.4)	194	500	19
ERH	Erhai Lake, China	Discrete	109	4.5	–	(–6.2)	–4.6	98	500	20
ERL	Erlongwan Lake, China	Smoothed	81	3.5	–	17.5	(19.2)	–15	335	21
ESC	Lake Escondido, Argentina	Smoothed	106	3.5	6.0	–2.8	–	25	300	22,23
FAN	Lake Fangshan, China	Smoothed	114	3.6	–	(1.0)	4.4	–139	500	24
FIN	2 Finnish Lakes, Finland	Smoothed	190	2.5	–	–0.4	(4.0)	–74	400	25
FIS	Fish Lake, Oregon, USA	Discrete	145	4.1	–	–2.2	(–1.9)	119	500	26
FRG	Frängsjön, Sweden	Discrete	161	3.8	7.9	–2.1	(3.2)	–163	450	27,28
FUR	Furskogstjärnet, Sweden	Discrete	174	4.1	8.0	2.0	(3.9)	207	500	28,29
GAR	Gardar Drift, North Atlantic	U-channel	168	3.5	7.4	(–14.3)	–19.9	159	500	30
GEI	Llyn Geirionydd, Wales, UK	Smoothed	128	3.5	–	1.0	(2.8)	80	300	31
GHI	Cape Ghir, NW Afr. Margin	Discrete	117	4.3	6.3	–0.8	(2.8)	361	500	32
GNO	Lake Gnotuk, Western Victoria, Australia	Discrete	135	4.0	–	–2.0	(1.5)	–21	300	16
GRE	Greenland, North Atlantic	U-channel	162	3.5	–	8.0	(6.5)	144	450	33
HUR	Lake Huron, Great Lakes, USA	Discrete	178	4.5	–	5.7	(9.1)	82	500	34
ICE	Iceland, North Atlantic	U-channel	174	3.5	–	–1.1	(–13.6)	103	300	33
JON	Jonian Sea, Italy	U-channel	58	3.5	–	–4.5	(–1.2)	361	500	2
KEI	Lake Keilambete, Western Victoria, Australia	Discrete	175	3.3	–	–0.8	(1.1)	52	200	16
KYL	Kylen Lake, Minnesota, USA	Discrete	60	4.2	–	(15.6)	17.0	218	500	35
LAM	Lake Lama, Siberia, Russia	Discrete	182	4.4	–	–9.0	–	–60	500	36
LEB	Lake LeBoeuf, USA	Smoothed	88	3.5	6.8	(0.8)	2.8	122	300	37
LOM	Loch Lomond, Scotland, UK	Smoothed	122	3.5	–	(–0.8)	–0.1	–109	300	38
LOU	Louis Lake, Wyoming, USA	Discrete	27	5.0	–	6.4	(5.5)	36	260	39
LSC	Lake St. Croix, Minnesota, USA	Discrete	152	4.0	6.9	–0.3	(–1.7)	141	500	35
MAR	Mara Lake, British Columbia, Canada	Smoothed	106	3.5	–	0.5	(1.8)	–171	500	40
MEE	Meerfelder Maar, Germany	Discrete	187	5.9	–	1.5	(5.6)	379	500	41
MEZ	Lago di Mezzano, Italy	Discrete	105	3.7	7.5	(1.6)	0.7	78	300	42
MNT	Lago Morenito, Argentina	Smoothed	176	3.5	–	5.1	–	37	300	17
MOR	Lac Morat, Switzerland	Discrete	35	3.2	–	(3.9)	4.5	97	180	3
MOT	Mötterudstjärnet, Sweden	Discrete	163	4.1	7.8	–1.8	(3.3)	48	390	28,29
NAU	Nautajärvi, Finland	Discrete	185	4.1	8.1	–6.8	(–1.7)	–39	400	28,43
PAD	Palmer Deep, Antarctic Peninsula	U-channel	165	3.6	7.3	–4.3	–	–7	300	44
PEP	Lake Pepin, USA	U-channel	146	3.5	6.3	–	–	49	250	45
POH	Pohjajärvi, Finland	Discrete	66	3.8	9.5	(0.6)	9.2	–80	390	46
POU	Lake Pounui, North Island, New Zealand	Smoothed	41	3.5	–	4.1	(–3.3)	12	180	47
SAG	Saguenay Fjord, Canada	U-channel	140	3.5	–	(1.1)	8.7	103	300	48
SAN	Hoya de San Nicolas, Mexico	Smoothed	113	3.5	–	3.7	(1.2)	6	100	49
SAR	Sarsjön, Sweden	Discrete	155	3.9	8.0	(–0.1)	2.0	–108	435	27,28
SAV	Savijärvi, Finland	Discrete	122	4.5	–	(–4.0)	1.6	–232	500	28,50
SCL	Lake Shuangchiling, China	U-channel	166	3.8	–	(26.4)	24.0	–24	500	51
STL	St. Lawrence Est., Canada	U-channel	150	3.5	6.6	19.0	(26.8)	–143	500	52
SUP	Lake Superior, Great Lakes, USA	Smoothed	184	3.6	–	4.0	(8.3)	–105	400	53
TRE	Laguna el Trebol, Argentina	Smoothed	141	3.5	5.8	7.9	–	18	240	54,55
TRI	Lake Trikhonis, Greece	Discrete	133	2.9	–	–2.4	(1.4)	243	500	11

Table 1 (Continued).

Abb.	Location	Sample type	N_{bin}^a	α_{63}^b (°)	s_F^b (μT)	ΔD_{MOD}^c (°)	ΔD_{ARC}^c (°)	ΔT_{AVG}^d (yr)	ΔT_{MAX}^d (yr)	Ref. ^e
TUR	Lake Turkana, Kenia	Discrete	51	4.1	–	–	–	–131	400	56
TY1	Tyrrhenian Sea, Italy	U-channel	61	3.5	–	–0.6	(–1.5)	119	500	2
TY2	Tyrrhenian Sea, Italy	U-channel	79	3.5	–	–0.5	(0.5)	190	450	2
VIC	Lake Victoria, Uganda	Smoothed	143	3.5	–	–	–	–10	150	57
VOL	Lake Volvi, Greece	Discrete	50	2.9	–	–1.9	(1.5)	265	500	11
VUK	Vukonjärvi, Finland	Discrete	102	4.1	–	–25.2	(–15.5)	225	500	58
WA1	PS69/274–1, West Amundsen Sea	Discrete	16	–	9.3	–	–	41	385	59
WA2	PS69/275–1, West Amundsen Sea	Discrete	18	–	9.1	–	–	316	500	59
WA3	VC424, West Amundsen Sea	Discrete	27	–	8.8	–	–	104	400	59
WAI	Lake Waiau, Hawaii, USA	Smoothed	109	3.5	–	–3.1	(–3.4)	–45	385	60
WIN	Lake Windermere, Northern England, UK	Smoothed	137	3.5	–	–3.9	(–2.5)	296	500	31
WPA	West Pacific, West Pacific	U-channel	187	3.5	–	–	–	185	450	61

^aNumber of bins after resampling.

^bMean α_{63} and s_F of binned data used for modeling.

^cDeclination adjustment (ΔD) based on prior dipole field model (MOD) or archaeomagnetic data (ARC). Adjustments not used are shown in brackets.

^dAverage and maximum timescale adjustments (ΔT), see Section 3.2.

^e1, Lisé-Pronovost *et al.* (2009); 2, Vigliotti (2006); 3, Hogg (1978); 4, Nourgaliev *et al.* (2003); 5, Nurgaliev *et al.* (1996); 6, Peck *et al.* (1996); 7, Thouveny & Williamson (1988); 8, Constable & McElhinny (1985); 9, Constable (1985); 10, Barletta *et al.* (2008); 11, Creer *et al.* (1981); 12, Frank *et al.* (2002b); 13, Frank *et al.* (2003); 14, Ali *et al.* (1999); 15, Hayashida *et al.* (2007); 16, Barton & McElhinny (1981); 17, Creer *et al.* (1983); 18, Frank *et al.* (2007); 19, Stockhausen (1998); 20, Hyodo *et al.* (1999); 21, Frank (2007); 22, Gogorza *et al.* (2002); 23, Gogorza *et al.* (2004); 25, Haltia-Hovi *et al.* (2010); 26, Verosub *et al.* (1986); 27, Snowball & Sandgren (2002); 28, Snowball *et al.* (2007); 29, Zillén (2003); 30, Channell *et al.* (1997); 31, Turner & Thompson (1981); 32, Bleil & Dillon (2008); 33, Stoner *et al.* (2007); 34, Mothersill (1981); 35, Lund & Banerjee (1985); 36, Frank *et al.* (2002a); 37, King (1983); 38, Turner & Thompson (1979); 39, Geiss *et al.* (2007); 40, Turner (1987); 41, Brown (1981); 42, U. Frank pres. comm.; 43, Ojala & Saarinen (2002); 44, Brachfeld *et al.* (2000); 45, Brachfeld & Banerjee (2000); 46, Saarinen (1998); 47, Turner & Lillis (1994); 48, St-Onge *et al.* (2004); 49, Chaparro *et al.* (2008); 50, Ojala & Tiljander (2003); 51, Yang *et al.* (2009); 52, St-Onge *et al.* (2003); 53, Mothersill (1979); 54, Gogorza *et al.* (2006); 55, Irurzun *et al.* (2006); 56, Barton & Torgersen (1988); 57, Mothersill (1996); 58, Huttunen & Stober (1980); 59, Hillenbrand *et al.* (2010); 60, Peng & King (1992); 61, Richter *et al.* (2006).

2.4 Calibration of sedimentary declination data

Sediment cores are usually azimuthally unoriented and palaeomagnetic declination data measured on sediments are therefore mostly published as relative values, calculated by removing the average over the whole sequence. While in many cases this approach will lead to reasonable results, there is a risk of introducing systematic errors to the data. The cores could potentially be oriented by fitting the declination data from the top of the sequence to historical field measurements (Constable *et al.* 2000), or alternatively to palaeomagnetic measurements of nearby lava flows correlated in time via tephra layers associated with the same eruption (Verosub *et al.* 1986). However, the sediments from the top of the core or next to tephra layers are often not ideal recorders of the geomagnetic field and therefore such adjustments could be problematic. Another problem is that the data published as relative declination are frequently provided to the database as absolute values (i.e. before removing the long-term average) and may therefore be mistaken for oriented data. To reduce any systematic errors introduced to the database by such type of core reorientations, or lack of reorientations, we adjust each sedimentary declination record by a constant number of degrees based on comparisons with the prior dipole field model or, when appropriate, archaeomagnetic data.

For each record, a first correction was determined as the median difference between the prior dipole model prediction and the data. Archaeomagnetic data were then selected from within a radius of 3000 km from each site and relocated using virtual geomagnetic poles (VGPs). Both the sedimentary and the archaeomagnetic declination data were smoothed with a 200-yr moving window at 100-yr intervals and if there were enough overlapping data points (at least 10), a second correction was determined as the median difference between the smoothed data. The smoothing of the data produces

more stable adjustments by restricting the comparison to the more robust long-term variations. To avoid corrections based on spurious data the second correction constant was used only in cases when the archaeomagnetic data provided a better fit to the data than the dipole field model, calculated as the mean of the absolute residuals. The difference between the adjustments predicted by the prior model and the archaeomagnetic data in regions where both could be determined is on average around 3.4° (Fig. 1). A summary of all adjustments can be found in Table 1.

The choice of a suitable radius for the selection of archaeomagnetic data is a trade-off between obtaining enough data used to calculate the adjustment while limiting the selection to an area with similar geomagnetic field history. A 3000 km radius can be considered quite large, however; given the Earth's ~40 000 km circumference, the corresponding 6000 km wavelength translates to spherical harmonic degree 6–7, which is roughly the spatial resolution of our final models (see Fig. 5). We found that the corrections calculated based on a smaller radius often lead to regionally inconsistent adjustments, mainly because of an over-reliance on individual archaeomagnetic data points. The declination adjustments based on a 3000 km radius produce a regionally consistent data set, which differ slightly but systematically from the predictions of the prior dipole field model (Fig. 1c).

2.5 Scaling of relative palaeointensity

The sedimentary relative palaeointensity data were converted to absolute palaeointensities, following the approach of Korte & Constable (2006) and Donadini *et al.* (2009), by multiplying each entire record with a constant scaling factor. As for the declination data, the scaling factor was calculated based on the prior dipole field model or using archaeomagnetic intensity data, where possible. The

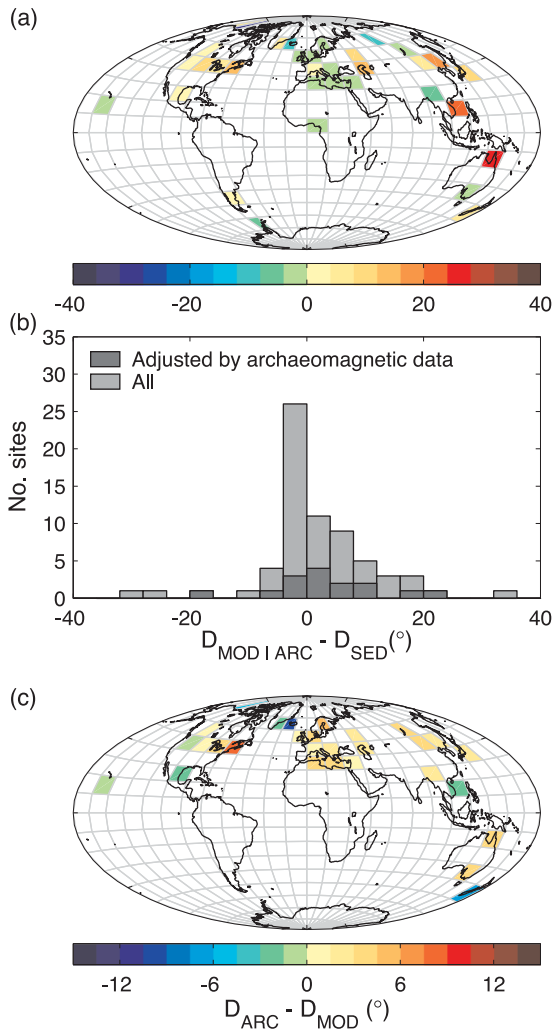


Figure 1. The mean difference between the declination predicted by either regional archaeomagnetic data (D_{ARC}) or the dipole prior (D_{MOD}) and the declination from each sediment record (D_{SED}) over overlapping time intervals. Upper panel (a and b) shows the mean difference determined for all records within each grid-cell and lower panel (c) shows the mean difference between adjustments determined using archaeomagnetic data and the dipole prior within each grid, where applicable.

scaling factor was determined as the median ratio of the reference palaeointensity data over the relative palaeointensity data.

For each record, a first scaling factor was determined based on the prior dipole field model. The archaeomagnetic data were selected using the same criteria as for the declination adjustments and smoothed using the same 200-yr moving window and used to calculate a second scaling factor. As for the declination corrections the second scaling factor was only used when the archaeomagnetic data provided a better fit to the data than the prior dipole field model, calculated as the mean of the absolute residuals. The scaling factors calculated based on the prior dipole model did not differ considerably (on average 4.5 per cent) from those based on archaeomagnetic data.

Relative palaeointensity reconstructions can be sensitive to changes in the depositional environment through time and such changes could lead to different scaling factors being appropriate for different parts of the sequence. In two cases (LSC at 600 BC and TRE at 0 AD), we found sudden jumps in the data that we identified as such changes in the depositional environment. In both cases sus-

piciously large changes in the relative palaeointensity could also be traced back to similar changes in concentration dependent mineral magnetic parameters at corresponding depths in the original studies (Lund & Banerjee 1985; Gogorza *et al.* 2006). To avoid applying inappropriate scaling factors both records were split into two parts, which were rescaled separately and then joined back together. We suspect that other relative palaeointensity records may suffer from similar problems, potentially with more gradual changes making them more difficult to identify. Improvements in both the identification and correction of this problem should be investigated in future studies.

2.6 Assigning error estimates

Uncertainty estimates of palaeomagnetic data are often poorly defined and sometimes not provided at all. Mostly this is because there are too few measurements to allow a precise estimate of the dispersion, but additionally unknown systematic errors also appear to be important, particularly for palaeointensity data (Suttie *et al.* 2011). As discussed by Korte *et al.* (2005) and Donadini *et al.* (2009) the published error estimates come from a wide array of different analyses and forms. The norm is to give uncertainty estimates in terms of the α_{95} confidence circle of the direction (Fisher 1953), and the standard deviation (σ_F) of the intensity measurements. The α_{95} is conveniently converted to a standard angular error (α_{63}) using

$$\alpha_{63} = \frac{81}{140} \alpha_{95}. \quad (1)$$

For the purposes of constructing a global field model it is important to use consistent uncertainty estimates to weight the individual data. To address these problems Donadini *et al.* (2009) assigned a minimum α_{63} error of 2.5° (3.5°) for archaeomagnetic (sedimentary) directional data and a minimum σ_F of $5 \mu\text{T}$ for all intensity data. These estimates, which were also assigned to data with unknown error estimates, were based on the average deviation of the data from the *gufm1* historical model between 1590 and 1990 AD. Using smoothing spline fits devised to capture the robust variation of each record Panovska *et al.* (2012) concluded that the minimum errors assigned to the sedimentary data by Donadini *et al.* (2009) are probably too small. In an effort to favour high-quality data Licht *et al.* (2013) opted to keep the original error estimates, when available, and instead introduced a modelling error of $\alpha_{63} = 2^\circ$ for directions and $\sigma_F = 2 \mu\text{T}$ for intensity, which was added in quadrature to the data uncertainty. They argued that although high-quality data cannot be fitted too closely by the model this limitation is mainly related to the limited resolution of the model and not the data uncertainty. To penalize data with unknown uncertainty Licht *et al.* (2013) assigned a root mean square (rms) value of all available published errors for each data type multiplied by a factor of 1.5.

In this study, we acknowledge that the published error estimates may fail to account for unknown systematic errors and have therefore opted for an approach similar to that of Donadini *et al.* (2009) using a set of minimum error estimates. However, to penalize data with less well-defined uncertainties, different minimum errors were assigned depending on the number of samples/specimens (N/n) used to calculate the mean direction or intensity.

Archaeomagnetic directions were assigned with a minimum $\alpha_{63} = 2.5^\circ$ for $N \geq 5$, $\alpha_{63} = 3.5^\circ$ for $N < 5$ and $\alpha_{63} = 4.5^\circ$ for data with unknown uncertainties. Because most archaeomagnetic directions are determined using at least five samples, we chose to also use a minimum $\alpha_{63} = 2.5^\circ$ for data where N was unspecified. For archaeomagnetic intensities we first converted the σ_F to standard errors of the mean (s_F), which is more consistent with the

treatment of the directional uncertainties, using

$$s_F = \frac{\sigma_F}{\sqrt{n}}, \quad (2)$$

where n is the number of specimens. Given enough data s_F should provide a good estimate of the experimental error. However, as noted by Suttie *et al.* (2011) the published errors appear to account only for a small fraction of the actual error budget, which is implied by the usual choice of σ_F as the uncertainty. Through direct comparisons with *gufm1* Suttie *et al.* (2011) suggested an appropriate minimum error in the range of 10–15 per cent of the true field strength. Expressing the error in terms of a percentage of the true field, rather than a fixed value of for example 5 μT , would have the advantage of not underweighting data from lower latitudes where the field is weaker, if uncertainties are proportional to field intensity. Based on these observations the intensity data were assigned with minimum $s_F = 10$ per cent for $n \geq 5$, $s_F = 12$ per cent for $n < 5$ and $s_F = 14$ per cent for unknown uncertainties. The true field strength at a given location and time was approximated using predictions of the prior dipole field model.

The sedimentary directional data consist of discrete sample measurements (31 records), different forms of running averages (25 records) and u-channel measurements (17 records). The data, especially from the second group, are sometimes published with some form of uncertainty estimate. However, out of all these records only 10 are provided with an error estimates in the database. These come in the form of α_{95} confidence limits (2), (angular) standard deviations (4) and maximum angular deviations (4). In order to treat the data consistently only the first were deemed suitable for the modelling purposes. These α_{95} confidence limits are based on stacks of 12 (EIF) and 8 (FIN) parallel cores with equivalent α_{63} rms values of 3.05° and 1.88° , respectively. While these errors may not be representative of all sedimentary data, the latter study (Haltia-Hovi *et al.* 2010) in particular highlights the potential precision with which the directions can be acquired given enough data. Based on the assumption that most hidden or systematic errors associated with sedimentary data are due to chronologic uncertainties, which are dealt with separately in Section 3.2, and problems with core orientation, partly solved by the declination adjustments, we treat error estimates in a similar way to the archaeomagnetic errors.

For the purpose of error assignment the sedimentary data can be divided into two groups: (i) records containing independent data from discrete samples and (ii) smoothed records (including u-channels) containing non-independent data. From the resampling of the data we obtain uncertainty estimates for both directions and rescaled intensities based on the dispersion of the data within each 50-yr bin. For data from the first group, with no prior error estimates, the resulting uncertainty estimates are treated in the same way as the archaeomagnetic data using the same minimum α_{63} and s_F assigned based on the number of samples used to calculate the mean values. For the data from the second group information is missing regarding both the number of independent data points and the true dispersion of the data. The provided α_{95} estimates from EIF and FIN were converted to α_{63} and transferred to binned error estimates through error propagation. Data from these two records were then assigned a minimum $\alpha_{63} = 2.5^\circ$ while the uncertainty estimates, calculated from the binned data, from the remaining records were treated as less well defined and assigned a minimum $\alpha_{63} = 3.5^\circ$. None of the rescaled intensity error estimates from the second group provided in the database were deemed suitable and therefore all uncertainty estimates, calculated from the binned data, were assigned a minimum $s_F = 12$ per cent. The strategy used here to assign uncer-

tainties to sedimentary data results in larger errors on average for both directions (3.8°) and intensities (7.1 μT) compared to the minimum values of 3.5° and 5 μT assigned by Donadini *et al.* (2009). However the methodology also allows for slightly smaller error estimates: 10 per cent of the α_{63} are smaller than 3.5° and 11.5 per cent of the s_F are lower than 5 μT . The average α_{63} and s_F from each record are listed in Table 1.

For the modelling procedure we want to treat inclination and declination separately. This is particularly important for the sedimentary data where each component might be associated with independent errors, such as core rotation affecting declination data and sediment compaction affecting the inclinations. Consequently all α_{63} error estimates were converted to inclination errors ($s_I = \alpha_{63}$) and to declinations errors (s_D) using

$$s_D = \frac{\alpha_{63}}{\cos I}, \quad (3)$$

where I is the inclination. Age uncertainties (σ_A) for archaeomagnetic data, derived from GEOMAGIA50, were assigned a minimum value according to the age of the sample ($\sigma_A = 100$ yr prior to 1000 AD, $\sigma_A = 50$ yr from 1000 to 1700 AD and $\sigma_A = 0$ yr from 1700 AD to present) to avoid overestimating the error of historical data. Archaeomagnetic data with unknown age uncertainties were assigned with the same minimum σ_A plus 50 yr. Sedimentary age uncertainties are more difficult to quantify for individual samples as they are usually derived from some form of interpolation between a few dated levels in the sediment column. Additional unknown uncertainties such as ‘old’ carbon ‘diluting’ the contemporary ^{14}C in the sediments (Björck & Wohlfarth 2001), potential hiatuses in the stratigraphy and lock-in delays of the remanent magnetization (Roberts & Winklhofer 2004) further complicate the age determination. To deal with these problems we have introduced a new way of treating the age uncertainties of sedimentary data in which all records are treated equally, see Section 3.2.

3 MODELLING METHOD

3.1 Initial model

The pfm9k models are constructed using an expansion on a spherical harmonic basis in space and cubic B-splines in time. The methodology follows that of Bloxham & Jackson (1992) used for historical field models and adapted for archaeomagnetic and palaeomagnetic data by Korte & Constable (2005, 2011) and Korte *et al.* (2009). We assume an electrically insulating mantle and neglect crustal fields and external (ionospheric and magnetospheric) fields. The time-dependent geomagnetic field, $\mathbf{B}(t)$, is described as the negative gradient of a scalar potential $V(t)$ everywhere outside the Earth’s core.

$$\mathbf{B}(t) = -\nabla V(t). \quad (4)$$

This potential can be expanded as a series of spherical harmonics

$$V(r, \theta, \phi, t) = a \sum_{l=1}^{l_{\max}} \sum_{m=0}^l \left(\frac{a}{r}\right)^{l+1} [g_l^m(t) \cos(m\phi) + h_l^m(t) \sin(m\phi)] \times P_l^m(\cos \theta), \quad (5)$$

where (r, θ, ϕ) are spherical polar coordinates (r is the radius from Earth’s centre, θ is the colatitude and ϕ is the longitude), t is time, $a = 6371.2$ km (the mean radius of the Earth’s surface) and l_{\max} is the truncation point of the expansion in spherical harmonics. The $P_l^m(\cos \theta)$ are Schmidt quasi-normalized associated Legendre

functions of degree l and order m . The structure of the field is defined by the time-dependent Gauss coefficients $\{g_l^m; h_l^m\}$, which are expanded on a basis of N cubic B-splines, M ,

$$g_l^m(t) = \sum_{n=1}^N g_l^{m,n} M_n(t) \quad (6)$$

with a similar expansion for h_l^m .

The spherical harmonic basis is expanded to degree 10 and the knot space is chosen as 50 yr. However, the actual ST resolution of the model will be lower and is determined by data and regularization. To find the smoothest, simplest model that satisfactorily fits the data we minimize the misfit to the data and two model norms, one measuring the roughness in the spatial domain and one in the temporal domain. For the spatial norm we use the physically motivated lower bound on Ohmic dissipation (Gubbins 1975) at the core mantle boundary (CMB; $r = c$), given by

$$\Psi = \frac{4\pi}{t_e - t_s} \int_{t_s}^{t_e} f(B_r) dt \quad (7)$$

with

$$f(B_r) = \sum_{l=1}^{l_{\max}} \frac{(l+1)(2l+1)(2l+3)}{l} \left(\frac{a}{c}\right)^{2l+3} \sum_{m=0}^l [(g_l^m)^2 + (h_l^m)^2]. \quad (8)$$

For the temporal norm we use

$$\Phi = \frac{1}{(t_e - t_s)} \int_{t_s}^{t_e} \oint_{\text{CMB}} (\partial_t^2 B_r)^2 d\Omega dt \quad (9)$$

where $[t_s, t_e]$ is the time interval over which we solve the field.

The coefficients from eq. (6) are represented by a model vector $\mathbf{m} = (g_1^{0,1}, g_1^{1,1}, h_1^{1,1}, \dots, g_1^{0,2}, \dots)$. The palaeomagnetic data, directions and intensity, are non-linearly related to the coefficients and we therefore have to find a solution iteratively from linearized equations. We use a constant axial dipole of $g_1^0 = 30 \mu\text{T}$ as a starting model, convergence is reached quickly and we always choose the 5th iteration as the final model. The resulting objective function to be minimized is

$$(\gamma - \mathbf{f}\mathbf{m})^T \mathbf{C}_e^{-1} (\gamma - \mathbf{f}\mathbf{m}) + \lambda_s \Psi + \lambda_T \Phi, \quad (10)$$

where $(\gamma - \mathbf{f}\mathbf{m})$ is the residual vector given by the difference between data γ and model \mathbf{m} related through the operator \mathbf{f} according to eq. (4) and \mathbf{C}_e is the data error covariance matrix, with damping parameters λ_s and λ_T . Based on the argument that a dipole field is a better smooth field assumption than a zero field (Korte *et al.* 2009), we exclude the dipole terms from the spatial regularization.

The damping parameters for the preferred model were chosen by visual comparison (Lodge & Holme 2009) of the time-averaged geomagnetic power spectra of the main field and secular variation to those of the historical field model *gufm1* and the high resolution palaeomagnetic field model CALS3k.4 (Korte & Constable 2011), respectively. The chosen regularization norms result in relatively stronger damping of power in main field and secular variation for higher spherical harmonic degrees (i.e. small-scale/short-term structure) compared to lower spherical harmonic degrees. We assume that a reasonable solution does not show more spatial complexity on average than the historical field and λ_s is chosen using the average main field power spectra of *gufm1* as a template. We attempt to preserve, or avoid exceeding, the relative proportions of the power spectra by limiting the ‘allowed’ power in each spherical

harmonic degree based on the power of lower spherical harmonic degrees, according to the *gufm1* power spectrum. Given the large dating uncertainties associated with the palaeomagnetic data, we also assume that a reasonable solution will not be able to capture variations on timescales shorter than 300–400 yr. To produce a suitable template for the secular variation power spectra based on this criterion we filter the CALS3k.4 Gauss coefficients with a 350-yr running average and λ_T is chosen by comparison to the average secular variation power spectrum of this temporally smoothed version of the CALS3k.4 model.

The models were built iteratively in several steps: (i) first a preliminary model A was constructed based on all data with the adjustments described above. (ii) A residual analysis was carried out and data lying more than three standard deviations in data uncertainty from the preliminary model predictions were rejected as outliers. Because the errors of the data are largely unknown we used the mean rather than the individual data uncertainty to identify data outliers. The mean data uncertainty was calculated independently for declination, inclination and intensity. To account for the greater variability of declination data associated with steeper directions, the declination errors (and residuals) used in the residual analysis were converted back to α_{63} using the inverse of (3)

$$\alpha_{63} = s_D \cos(I_p), \quad (11)$$

where I_p is the inclination of the model prediction. Following a similar argument, all intensity errors (and residuals) were normalized by the intensity predicted by the model. A new model B1 was constructed based on the outlier free data. (iii) The sediment declination data and relative palaeointensity records, based on the outlier free data set, were recalibrated using the B1 model and a third model C1 constructed.

The last two steps were repeated. After the first iteration 6.5 per cent of the declination data were rejected (cutoff = 11.15°), 6.4 per cent of the inclination data (cutoff = 10.62°) and 5.1 per cent of the intensity data (cutoff = 37.50 per cent). The absolute change in the declination and relative palaeointensity calibration factors after the first iteration were on average 1.9° and 2.9 per cent, respectively, with changes up to 8° (mainly high latitude sites) and 10 per cent required for some records. After the third iteration less than 0.2 per cent of the data were rejected and changes to the calibration factors were reduced to on average 0.2° and 0.3 per cent. The final model pfm9k.1 was chosen as model B3. To minimize end effects associated with the B-spline functions the model is determined for the period between 7500 BC and 2000 AD but we only show results from 7000 BC to 1900 AD. We decided to keep a relatively larger part of the recent end of the model in order to be able to validate the model against *gufm1*, even though this part of the model will include some spline end effects.

Regularized models will tend to underestimate, rather than overestimate, the intensity with respect to the data. This is true even if we exclude the dipole coefficients from the regularization, as can be seen in Table 2. The problem can be exacerbated by the inclusion of sedimentary relative palaeointensity records, particularly if they are rescaled using a model that is already underestimating the intensity. Including iteratively rescaled sedimentary data in the residual analysis may also produce near evenly distributed intensity residuals hiding the fact that the model is underestimating the absolute intensity data. This is partly resolved by resampling the sedimentary data, effectively increasing the weight of the archaeomagnetic, absolute, intensity data. To further improve the fit we also increased the weight given to all intensity data by 50 per cent, which was achieved by reducing the uncertainty estimates of the data accordingly during the inversion process. A similar approach

Table 2. Model-data residuals, archaeomagnetic data.

Model ^a	N_{ARC}^b	F_{AVG}^c	rms_F^d	$\text{rms}_{\text{ARC}}^d$
ARCH3k.1	10110	1.09	1.46	1.57
CALS10k.1b	12043	3.23	1.77	1.88
Dipole field prior	12043	-0.15	1.72	2.19
pfm9k.0 (initial)	12043	2.97	1.78	1.81
pfm9k.0 (dec. data adjusted)	12043	2.48	1.75	1.79
pfm9k.0 (sed. data resampled)	12043	1.16	1.64	1.69
pfm9k.1 (increase weight to F)	12043	0.66	1.58	1.69
pfm9k.1a (sed. timescales adjusted)	12043	0.72	1.58	1.68

^aDifferent pfm9k models listed with more data treatments (in brackets) added successively from top to bottom.

^bNumber of archaeomagnetic data (dec + inc + F) between -7000 and 1900 AD used for the residual analyses.

^cAverage intensity residuals ($F_{\text{DATA}} - F_{\text{PRED}}$).

^dThe rms of residuals for intensity and all data, normalized by their individual uncertainty estimates.

was used by Korte & Constable (2005), but with a 100 per cent increase in the weight. We found that a 50 per cent increase provided a good balance between improving the model fit to the intensity data, reducing the model underestimation, while not markedly changing the overall rms misfit to the data (including directions).

3.2 Addressing sediment age uncertainties

The age uncertainties of the data are often not well constrained and therefore applying a strong temporal damping seems a reasonable approach. This will be effective if the age uncertainties can be considered to be non-systematic, for example for the archaeomagnetic data where most data points have been dated individually. However, for the sedimentary data the age estimates can be both systematically wrong, for example due to reservoir effects affecting the radiocarbon dates, and have correlated errors due to the interpolation of ages when constructing an age depth model. Given the stratigraphic information of the data we can attempt to correct for this by finding an optimal age-depth model for each sedimentary record based on comparisons to a preliminary model prediction (Fig. 2). In regions where the model is not overly dependent on individual records this approach should be able to correct for inconsistencies in the data set that are due to incompatible age-depth models. In contrast, in regions where data are scarce this approach will result in few or no adjustments to the timescales. For this analysis we used the initial data set (before outlier rejection) and the pfm9k.1 model.

Based on an approach previously used by Nilsson *et al.* (2011) the individual timescales of the sedimentary records were randomly stretched and compressed, allowing for a maximum timescale adjustment of $T_{\text{lim}} = (\pm)500$ yr for each data point while still preserving the stratigraphic relationship. In practice these adjustments were achieved by dividing each timescale, from -7000 to 2000 AD, into 500-yr blocks. Using 2000 AD as a fixed starting point and moving back in time, each block was then randomly stretched or compressed by up to 30 per cent (using 50-yr steps) while keeping within the ± 500 yr limits of the original age estimates. To explore this rather large parameter space and to find the timescale adjustment that is most compatible with the model we use a nested sampling approach (Skilling 2006). Briefly explained we start off with a set of 50 randomly adjusted timescales. Each timescale adjustment is ranked by the χ^2 sum of the model-data residuals normalized by the data uncertainties

$$\chi^2 = \sum_i \frac{(D_s - D_{pi})^2}{s_{Di}^2} + \sum_j \frac{(I_j - I_{pj})^2}{s_{Ij}^2} + \sum_k \frac{(F_k - F_{pk})^2}{s_{Fk}^2}, \quad (12)$$

where D , I and F are the declination, inclination and intensity data and D_p , I_p and F_p the equivalent model predictions. Iteratively the worst ranking timescale is replaced by a variation of one of the 49 remaining timescales, if it results in an improved χ^2 . We found that 500 000 iterations was usually enough to isolate the best-fit timescale adjustment. After adjusting the timescales of all sediment records a new model, pfm9k.1a, was produced using the same approach and the same damping parameters used for pfm9k.1.

Adjusting the timescale is justified if it leads to a significantly better fit; in particular if the ratio of likelihoods exceeds a certain threshold. The log likelihood of the unadjusted data (L_0) and the adjusted data (L_A) can be expressed as

$$\log L_0 = c - \frac{\chi_0^2}{2} \quad (13)$$

and

$$\log L_A = c - \frac{\chi_A^2}{2}, \quad (14)$$

where c is some constant. To see if adjustment A is justified we calculate the odds. H is the hypothesis that the time should be left unchanged. Bayes theorem says the probability of H and A given data R , where $P(H)$ is the prior probability of H and $P(A)$ is the prior probability of A , are given by

$$P(H|R) = \frac{L_0 P(H)}{P(R)} \quad (15)$$

and

$$P(A|R) = \frac{L_A P(A)}{P(R)}. \quad (16)$$

We should prefer A over H if

$$\frac{P(A|R)}{P(H|R)} > 1 \quad (17)$$

or if

$$\log L_A - \log L_0 > \log \frac{P(H)}{P(A)}. \quad (18)$$

The ratio of prior probabilities is simply the size of the space that A was picked from (assuming a uniform prior for A). This is of the order 7^{18} for the maximum of 18 different blocks, each one which can be moved in up to seven different ways with respect to the adjacent block. Therefore, the time adjustment is justified if

$$\frac{\chi_A^2}{2} - \frac{\chi_0^2}{2} > N_{\text{blocks}} \log 7. \quad (19)$$

We find that this condition is satisfied for about 90 per cent of the records (the remaining 10 per cent are mostly represented by records where the analysis resulted in only minor timescale adjustments) and therefore conclude that the timescale adjustments can be considered justifiable.

In Fig. 2, we show examples from three different records of data plotted against their original timescales and the optimally adjusted timescales compared with predictions of the pfm9k.1 model. All three records show time adjustments of 300 yr or more, both towards younger and older ages. The top 4000 yr from the Fish Lake record (FIS) has been shifted on average 288 yr towards younger ages. This is supported by a similar adjustment of ~ 280 yr which was suggested by Hagstrum & Champion (2002), due to calcium carbonate dilution of the bulk ^{14}C samples used to date the record. The Fish Lake chronology was also forced to fit an independent age estimate of the Mazama Tephra layer, of about 4800 BC

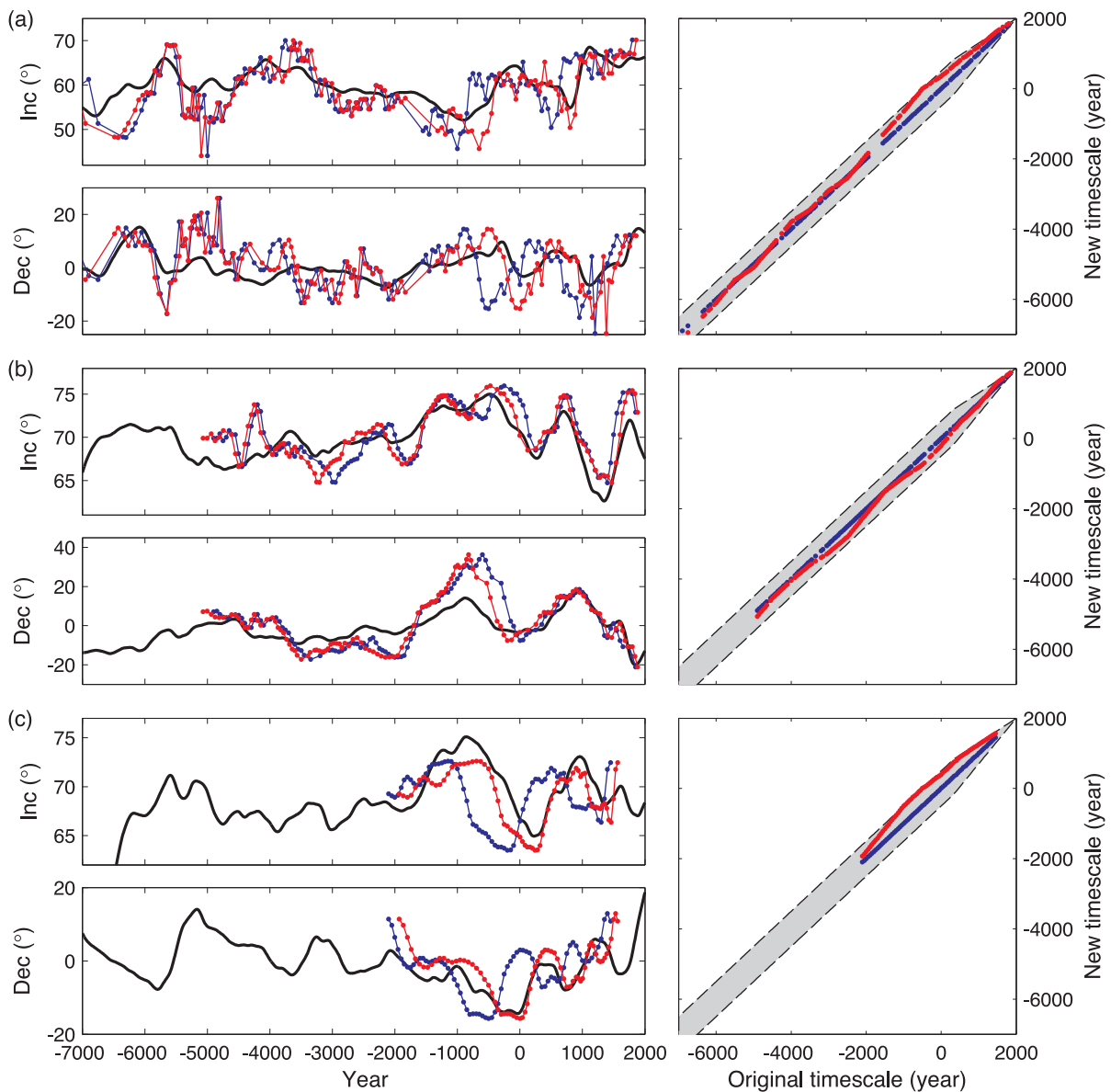


Figure 2. Example of timescale adjustments, shown for (a) Fish Lake, (b) Loch Lomond and (c) Lake Aslikul. For each example the subplots are organized as follows: Inclination (upper left), declination (lower left) and timescale (right). Original timescale (blue), adjusted timescale (red) and pfm9k.1 model prediction (black). The light grey shaded area shows the minimum and maximum allowed timescale adjustments.

(Verosub *et al.* 1986), which explains why the model predicts only minor time adjustments for this older part of the record. Fig. 3 shows the distribution of timescale adjustments defined as $\Delta T = T_{\text{adjusted}} - T_{\text{original}}$, where T is the age estimate of individual data points. Overall the distribution is slightly skewed towards younger ages, particularly for the last 3000 yr where the model is more heavily constrained by archaeomagnetic data. This could suggest either a widespread ‘old’ carbon problem affecting the radiocarbon based chronologies or possibly a predominant lock-in delay effect.

3.3 Addressing all data uncertainties

To investigate the effects of magnetic and age (MA) uncertainties as well as the impact of the ST distribution of the data we used the MAST bootstrap methodology, described in detail in Korte *et al.* (2009). First a temporary model pfm9k.1B was constructed based

on the same approach as above but with a more relaxed temporal damping, chosen by visual comparison to the secular variation power spectra of *gufm1*. For each of the 2000 bootstrap samples we created data sets by drawing on the final pfm9k.1B data set. The bootstrap models were constructed without further iterative recalibration or rejection of data and using the same damping parameters as for pfm9k.1B. The simulated data at each location were generated in two steps with slight differences for archaeomagnetic and sedimentary data. (i) In the first step the archaeomagnetic data were independently sampled from two normal distributions, one centred on the value of the magnetic component with a standard deviation corresponding to the data uncertainty estimate, and the other centred on the age estimate and using its respective standard error. For the sedimentary data the sampling of each datum from a normal distribution centred on the magnetic component was done in the same way. However, for the temporal sampling the timescale of each record was instead randomly stretched and compressed using

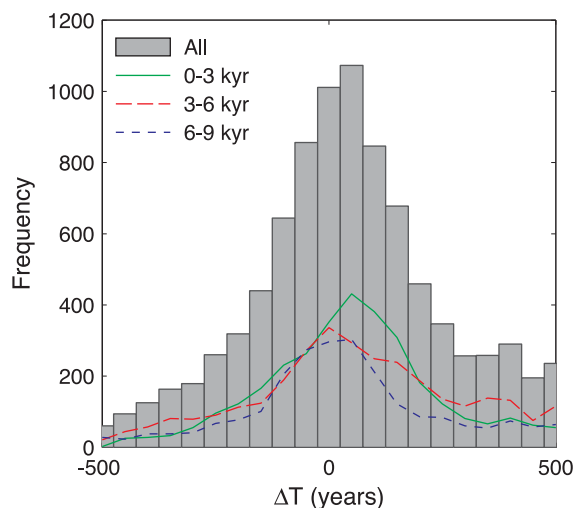


Figure 3. Histogram of all timescale adjustments made to the sedimentary data defined as $\Delta T = T_{\text{adjusted}} - T_{\text{original}}$, where T is the age estimate of individual data points. Also shown are the distributions of ΔT for the last 3000 yr (solid green line), between 4000 and 1000 BC (long dashed red line) and between 7000 and 4000 BC (short dashed blue line).

the same routine described above. This introduces rather large, but from what we can infer from the analysis in Section 3.2 also quite realistic, chronological errors that increase with age. (ii) In the second step, bootstraps were performed on these data sets, where for the archaeomagnetic data the number of data locations was kept constant and values picked by uniform random sampling from that data set. For the sediments, the number of records was kept fixed and the locations again uniformly sampled. The final model, pfm9k.1b, was based on the average of the 2000 bootstrap models and the uncertainties determined as standard deviation of the coefficients. The number of 2000 models was found to be enough to reach convergence.

4 MODEL RESULTS AND COMPARISONS

We have constructed three new models of the geomagnetic field variation for the last 9000 yr; (i) pfm9k.1 based on the initial data set with strong temporal damping, (ii) pfm9k.1a based on an optimally timescale-adjusted data set with strong temporal damping and (iii) pfm9k.1b: the average of 2000 bootstrap models with weak temporal damping.

4.1 Model-data comparisons

By reducing inconsistencies in the sedimentary age estimates, pfm9k.1a is able to capture larger amplitude palaeosecular variation (PSV) than other models that include sedimentary data, such as pfm9k.1b and CALS10k.1b (Fig. 4). The predictions of pfm9k.1a are in good agreement with models based on archaeomagnetic data, for example A_FM (Licht *et al.* 2013) and ARCH3k.1 (Korte *et al.* 2009), for the northern hemisphere sites where the latter models can be considered more robust. Well known PSV features such as the westward declination swing in Europe around 700 BC, between declination features ‘f’ and ‘e’ originally labelled by Turner & Thompson (1981), and the steep rise in inclination in North America around the same time tend to be smoothed out in models that incorporate sedimentary data. This is mainly due to the often relatively

large (up to 500 yr) inconsistencies between age estimates for sediment records from the same regions. We also note that in regions where the field is less well constrained, for example South America, the sediment timescale adjustments could potentially also amplify noise present in the pfm9k.1 model.

Resampling the sedimentary data has reduced the influence of data from a few overrepresented records and also given more weight to archaeomagnetic data. This is particularly noticeable in East Asia and South America where CALS10k.1b appears to be heavily dependent on two u-channel records (WPA and PAD). The strong influence of these two records in CALS10k.1b leads to an underestimation of intensity in East Asia for the last 2000 yr and causes a general underfitting to other data from the same region, seen in all three components (Fig. 4).

The effects of the declination adjustments are most obvious in East Asia and the SW Pacific where our new models, based on the adjusted data, do not show a similar persistent westward offset as predicted by CALS10k.1b (Fig. 4). As shown in Fig. 1 and Table 1, several declination records from both SW Pacific and East Asia required adjustments of more than 10° in the same direction (BAR, EAC, ERL and SCL). All of these corrections were either based on or are supported by comparisons to archaeomagnetic data, which would suggest that this systematic offset seen in the sedimentary declinations from this region is not a real feature of the geomagnetic field. On the other hand, the archaeomagnetic data from the SW Pacific are both few and scattered, as shown in Fig. 3, and we acknowledge that the declination adjustments applied to the data from this region are rather uncertain.

Time variation of the rms model-data residuals normalized by the data uncertainties for pfm9k.1a and pfm9k.1b are shown in Fig. 4 and a summary for all three models is provided in Table 3. The misfits are calculated on the respective outlier free data sets and therefore differ slightly from the values obtained in Table 2. Due to the relaxed temporal damping the outlier free data set of pfm9k.1b contains slightly more data than the pfm9k.1 data set and due to the adjustments of the sedimentary record timescales even fewer outliers are removed in the final pfm9k.1a data set. The pfm9k.1b model has considerably higher rms misfits than both pfm9k.1 and pfm9k.1a owing to the increased temporal smoothness. Not surprisingly the pfm9k.1a model has the smallest rms misfit of all models with the main improvements seen in the fit to the sedimentary data.

4.2 Dipole versus non-dipole field

The comparison of time-averaged main field power spectra in Fig. 5 reveals that all new models have less power in the quadrupole terms than both *gufm1* and CALS10k.1b (Fig. 5). In the case of CALS10k.1b this is mainly due to differences in g_2^0 and g_2^2 , which in turn appear to be related to the resampling of the sedimentary data and the declination adjustments. Due to the way we choose the damping parameters, attempting to preserve the relative proportions of the time-averaged *gufm1* power spectra, the new models also show similarly suppressed power in all higher degree terms. Based on end-to-end simulations using synthetic data sets Licht *et al.* (2013) found a general tendency of the models to underestimate the g_2^1 component. If the same applies to our new models, it could suggest that the observed low power in the quadrupole, relative to *gufm1*, is due to a bias in the data set. On the other hand, it is also possible that the power spectrum of the historical field is not representative of the field on longer timescales. In either case

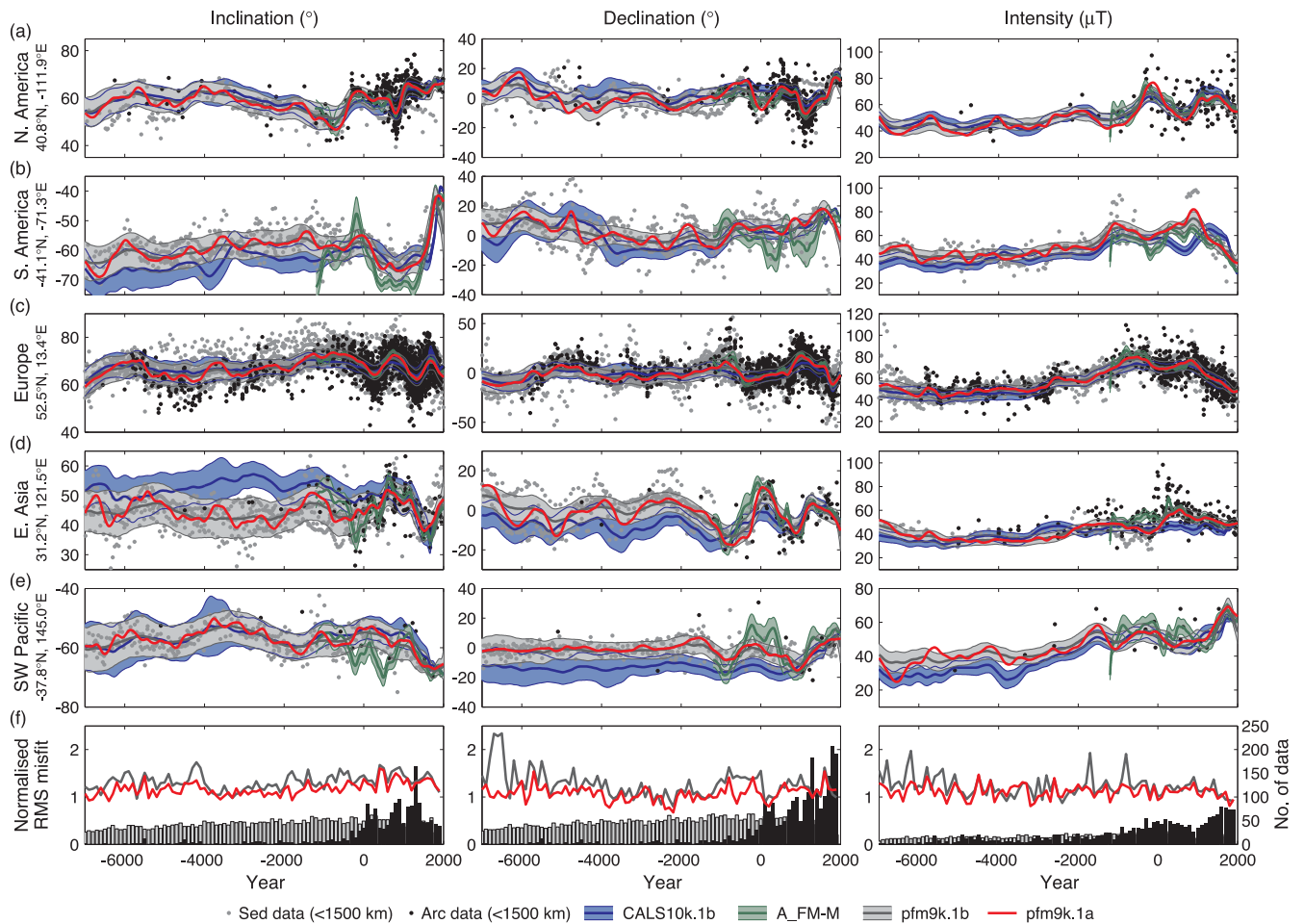


Figure 4. Examples of model predictions of declination (left), inclination (middle) and intensity (right) for five globally distributed locations (a–e) compared to timescale-adjusted sedimentary (grey) and archaeomagnetic data (black) from within a 1500 km, relocated based on an axial dipole. Note that the y-axes have been adjusted to capture the main variations in both model and data and may in some cases exclude extreme values. Bottom panel (f) shows the normalized rms misfits of pfm9k.1a and pfm9k.1b and the data distribution through time of the three different components.

Table 3. Model-data rms, final data sets.

Model	N_{ALL}^a	$\text{RMS}_{\text{DEC}}^b$	$\text{RMS}_{\text{INC}}^b$	RMS_{F}^b	$\text{RMS}_{\text{ARC}}^b$	$\text{RMS}_{\text{SED}}^b$	$\text{RMS}_{\text{ALL}}^b$
pfm9k.1	29051	1.15	1.27	1.14	1.27	1.16	1.20
pfm9k.1a	29422	1.09	1.23	1.12	1.26	1.08	1.16
pfm9k.1b	29207	1.26	1.36	1.21	1.34	1.26	1.30

^aNumber of data (dec+inc+F) between -7000 and 1900 AD used for the residual analyses.

^bThe rms of residuals for different data types and sources, normalized by their individual uncertainty estimates.

the power in the higher degree terms ($l > 2$) of the new models may have been excessively suppressed.

The time-averaged secular variation spectra of all three models are fairly similar to each other, with pfm9k.1b exhibiting slightly less power and pfm9k.1a slightly more power in degrees 1–4. The resulting temporal resolution of the models is estimated to 300–400 yr by comparing the power spectra of model predictions (declination, inclination and intensity) at different coordinates.

The dipole field variation, that is the movement of the north geomagnetic pole (NGP) and changes in dipole moment, of all three new models are fairly similar (Fig. 6). The largest variation is seen in pfm9k.1a but it rarely strays outside the pfm9k.1b one sigma confidence limit. Apart from a slight decrease in NGP colatitude around 1800 AD, all new models show quite good reproducibility

with NGP positions of the prior dipole field model for the last 400 yr (based on *gufm1*). The NGP movements of the new models are also in good agreement with the dipole field model for the earlier parts (based on DE_{FNKKE}), although mostly with slightly lower colatitudes. The NGP longitude of the new models and CALSt10k.1b diverge slightly between 4000 BC and 1500 AD, but in general the models agree well and the differences are within the uncertainty limits. All reconstructions, but particularly pfm9k.1a and the dipole field prior, suggests the presence of a 2700- or 1350-yr periodicity signal in the dipole tilt variation previously noted by both Nilsson *et al.* (2011) and Korte *et al.* (2011).

In common with the prior dipole field model and CALSt10k.1b the new models predict relatively low dipole moments around 6000 to 4000 BC increasing and reaching a maximum around 1000 BC to

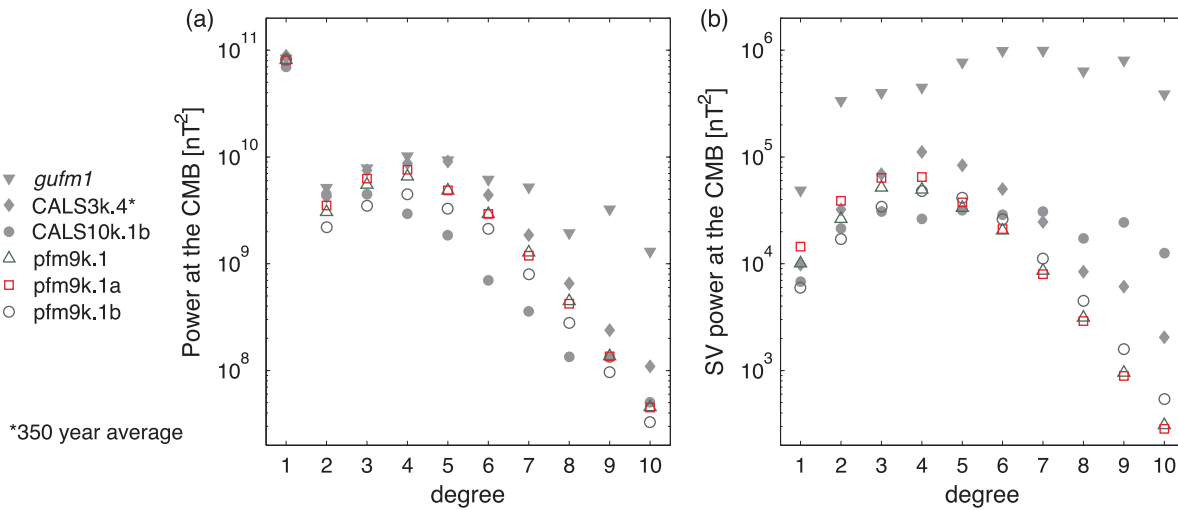


Figure 5. Time-averaged power spectra of (a) main field and (b) secular variation of the three new models (hollow symbols) and three other models shown for reference (grey solid symbols). The gauss coefficients of the CALS3k.4 were smoothed with a 350-yr running average prior to calculating the power spectra.

1000 AD (Fig. 6c). The new models predict on average higher dipole moments than CALS10k.1b for the earlier part of the record, where the models are more dependent on sedimentary data, but mostly agree within the uncertainty estimates. The dipole moments of the new models are also high when compared to prior dipole field model for the last 400 yr (based on *gufm1*), but predict roughly the same negative slope. By successively excluding different data types we found that this potential overestimation of the dipole moment for the recent end of the model is related to the introduction of sedimentary directional data. It is possible that the declination adjustment of a few records based on the dipole prior model may have forced the field to become more dipolar, however, this needs to be investigated further.

Fig. 6(d) shows the power of the sum of all the higher-degree, non-dipole, harmonics of the different models compared through time. The most striking feature is the relatively low non-dipolar field predicted by the new models between 4000 and 1500 BC. This coincides with the period where the NGP longitude deviates slightly from CALS10k.1b and is related to the adjustments made to the sedimentary data. Such low non-dipolar field appear unrealistic and indicates that the models may not be well constrained during this period in time.

4.3 Radial field at the core-mantle boundary

In Fig. 7, we compare time-averages/time-slices of B_r at the CMB for pfm9k.1a, pfm9k.1b and the most recent global models for three different time-periods. The structures shown by the new models and CALS10k.1b are similar for the long-term time-average, 7000 BC to 1900 AD (Fig. 7a). All three models show two high latitude areas that preferentially exhibit high intensity flux in the southern hemisphere, beneath South America and the Pacific Ocean, although the latter feature is slightly less pronounced in pfm9k.1b. In addition, both pfm9k.1a and pfm9k.1b show indications of two persistent high latitude high intensity flux patches in northern hemisphere, beneath Greenland and Western Russia. The northern and southern hemisphere high latitude flux patches are not symmetrically located around the equator. However, due to the poor data coverage for the southern hemisphere, the location of these flux patches are more uncertain. As pointed out by Licht *et al.* (2013), and as we will see in Section 5, there is a risk that the occurrence of these features

is related to a sampling bias. The new models show a less pronounced SW Pacific anomaly compared to CALS10k.1b due to the declination adjustments and the resampling of the sedimentary data. The persistent anomaly also has a different signature compared to CALS10k.1b, characterized by comparatively weaker flux beneath the Fiji islands.

The new models' time-averaged B_r for the last 3000 yr are characterized by more variable field structure in the northern hemisphere compared to the longer time average (Fig. 7b). There are three areas that preferentially exhibit high intensity fluxes beneath Greenland, Europe and Eastern Asia. Both pfm9k.1a and pfm9k.1b also exhibit generally more complex structure at high latitudes in the northern hemisphere compared to the recently published ASDI_FM-M model (Licht *et al.* 2013). The SW Pacific anomaly is again not as pronounced in the new models compared to both in CALS10k.1b and ASDI_FM-M, due to the above-mentioned adjustments of the sedimentary data. Instead the new models predict a persistent strong flux beneath East Asia.

Fig. 7(c) shows the B_r prediction at the CMB of the two models for the year 1900 AD compared to the prediction of *gufm1*. The northern hemisphere predictions of both models are relatively accurate but smoothed, roughly equivalent to the *gufm1* model prediction truncated at spherical harmonic degree 5–6 (see Fig. 8). The southern hemisphere reconstruction, on the other hand, provides much less higher order structure and is dominated by spherical harmonic degree 3–4. The two southern hemisphere high latitude high intensity flux patches present in *gufm1* are represented as one diffuse area of high flux in pfm9k.1a. The comparison provides a direct, although slightly limited, evaluation of how much structure we can expect the models to capture. We note that sedimentary palaeomagnetic data, which are particularly important for the southern hemisphere reconstruction, are poorly represented in the last few centuries of the database, mainly due to the difficulty in getting a reliable signal from the top sloppy part of sediment cores.

Fig. 9 shows five different time slices of the pfm9k.1a B_r at the CMB. We focus on the last 4000 yr where the model is best constrained. For a more complete illustration the reader is referred to the animations provided with the Supporting Information (Movies 1–3). Throughout the selected time period the southern hemisphere B_r prediction is characterized by the appearance and disappearance of two high latitude high intensity flux patches beneath

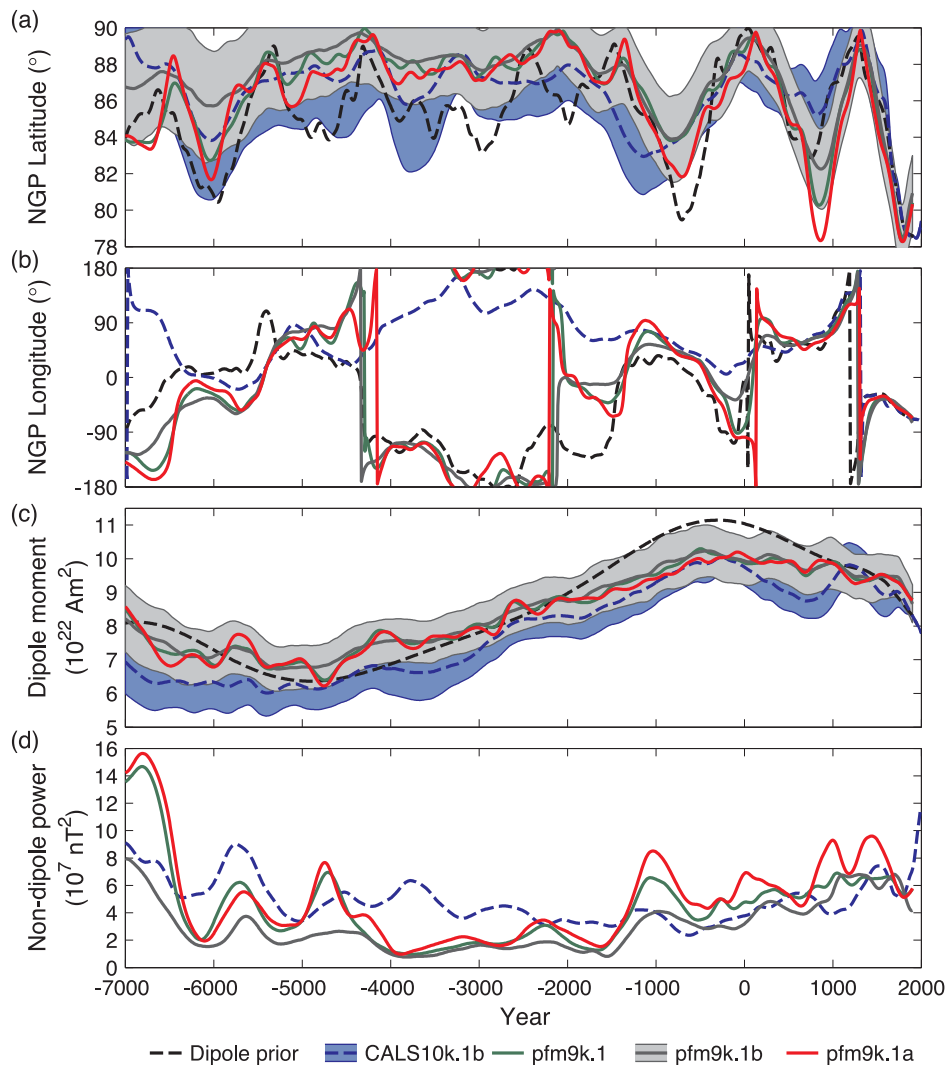


Figure 6. (a) North geomagnetic pole (NGP) latitude, (b) NGP longitude, (c) dipole moment and (d) sum of non-dipole field power of the dipole field prior (dashed black line), CALS10k.1b (dashed blue line), pfm9k.1 (green line), pfm9k.1b (grey line) and pfm9k.1a (red line). Uncertainty estimates from the bootstraps of CALS10k.1b (blue) and pfm9k.1b (grey) for NGP latitude and dipole moment are shown as light shaded areas. Note that some of the jumps in the NGP longitude, due to the circularity of the data, have been removed to make the figure clearer. The following sediment records were selected for each location (see Table 1 for full names): (a) FIS, LOU, MAR, (b) CAM, ESC, MNT, TRE, (c) AD1, AD2, ANN, BEG, BOU, EIF, FRG, FUR, GEI, LOM, MEE, MEZ, MOR, MOT, NAU, POH, SAR, SAV, TY1, TY2, WIN, (d) BI2, BIW, ERL, FAN, WPA, (e) BLM, GNO, KEI.

South America and the SW Pacific. There is not much movement between them and for the most part they are situated at the edge of the tangent cylinder. The B_r prediction for the northern hemisphere reveals a much more dynamic behaviour. The northern hemisphere structure is dominated by the presence of two, but sometimes three, high latitude high intensity flux patches which move with an overall westward motion around the edge of the tangent cylinder. The movement or disappearance/emergence of flux patches is heavily smoothed due to the strong temporal damping but appears to describe a stop-and-go motion with an average rate equivalent to a 5000-yr rotation period. The apparent westward high latitude flux motion correlates well with a more or less continuous westward movement of the NGP between -1800 and 600 AD (Fig. 6). The NGP then moves eastwards up to about 500 AD during which the high latitude flux motion breaks down and the field structure becomes more complex.

The field evolution at the CMB predicted by pfm9k.1a, in particular, also shows a recurrence of reversed (or weak) flux just

at the edge of the tangent cylinder in the northern hemisphere around -1500 , -300 , 700 and 1900 AD. These reversed flux patches appear in association with, and at the far side of, two high latitude high intensity flux patches predominantly situated in one hemisphere. In at least two cases (-300 and 1900 AD) they seem to originate from the equator and move northwards towards the edge and possibly into the tangent cylinder over a period of a few centuries. However, due to the truncation level of the models it may not be possible to track any movement into the tangent cylinder (see comparison with *gufm1* at different truncation levels, Figs 7–8).

5 EVALUATION OF MODELS USING *gufm1*

To investigate how well we can expect our models to resolve the field structure at the CMB we generated a set of synthetic data sets with the same data uncertainties and the same ST data distribution as the final outlier free pfm9k.1 data set. The synthetic data sets

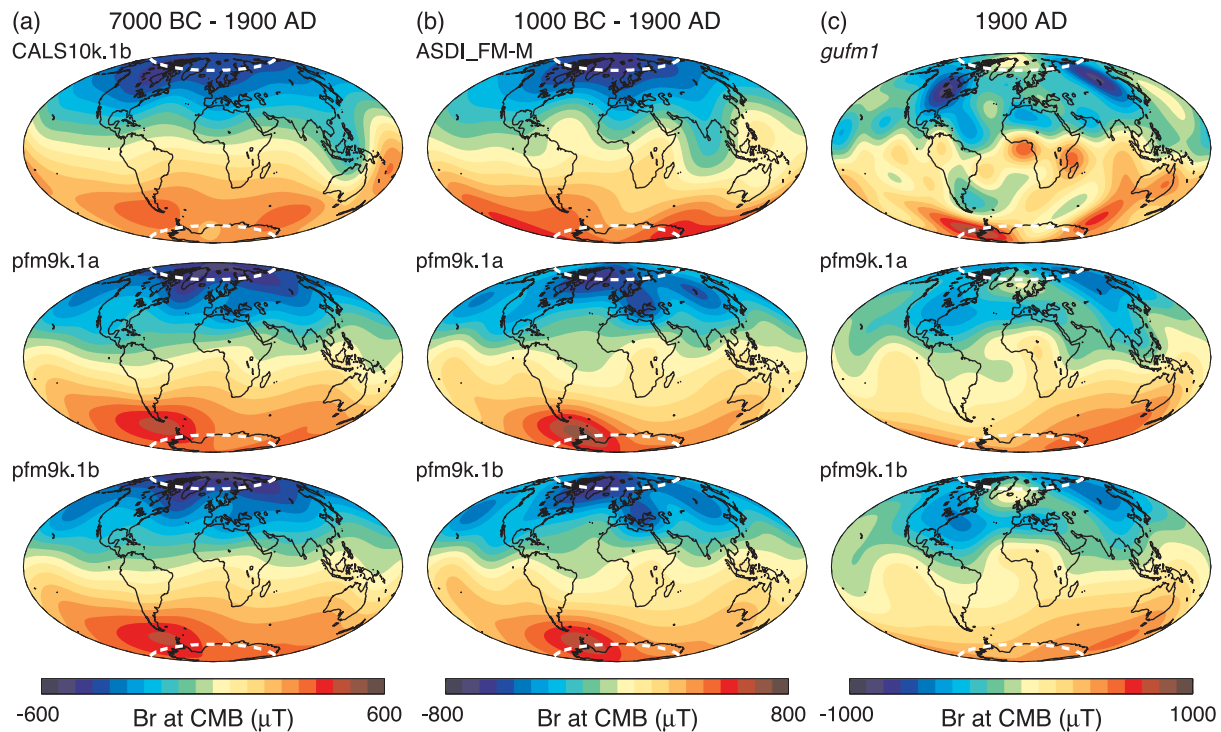


Figure 7. (Upper panel) Time-averaged radial component of the field (B_r) at the core mantle boundary (CMB) predicted by representative models for each time period: (a) CALSL10k.1b 7000 BC to 1900 AD, (b) ASDI_FM 1000 BC to 1900 AD and (c) *gufm1* 1900 AD. B_r predictions over the same time periods for pfm9k.1a (middle panel) and pfm9k.1b (lower panel). The dashed white lines show the CMB expression ($\sim 71^\circ$ N/S) of the inner core tangent cylinder.

were resampled in time and space from a reasonably realistic field description, a reference field model, covering the investigated time interval. MA data uncertainties were added in the same way as for the construction of pfm9k.1b, but with the distinction that the data age estimates were kept constant and age uncertainties were introduced to obtain the reference field model predictions. Finally, a new set of synthetic models was produced based on the synthetic data sets and the same damping parameters as for the final pfm9k.1 model. The model performance was evaluated by comparing the B_r at the CMB of the synthetic model and the reference field model.

The choice of a suitable reference field model is important and will to some degree influence the results. For a similar type of analysis Licht *et al.* (2013) used a periodically extended version of the *gufm1* model, covering the last three millennia. Here, we have instead opted to use single time-slices, also derived from the *gufm1* model, extended back in time by adding a continuous 5000-yr westward rotation to the whole field. The advantage of this approach is that it provides a direct test of the robustness of the observed westward drift pattern observed in the palaeofield models. An initial reference field model was constructed using the *gufm1* prediction at 1840 AD and extended backwards and forwards in time with a continuous westward rotation to cover the palaeofield model time period -7000 to 1900 AD. An animation showing the time variation of the B_r at the CMB for this reference field model and the corresponding synthetic model is provided in the Supporting Information (Movie 4).

Because of the nature of the regularization, to minimize field structure at the CMB, the model performance test will be more sensitive in areas where the reference field model shows more structure, for example in the vicinity of high intensity flux patches. To reduce the impact of such ST differences in a particular reference

field model we generated 1000 different reference field models and corresponding synthetic data sets. Each reference field model was constructed by randomly (i) varying the year (1590–1990 AD) used to select the initial *gufm1* time-slice, (ii) pre-rotating the field by 0 – 359° around the z-axis and (iii) occasionally reversing the polarity of the field solution before extending it backwards and forwards in time by adding the continuous westward rotation. 1000 solutions were found to be enough to reach convergence for the time-averaged B_r residuals. The rms of the B_r residuals at the CMB calculated for all 1000 different cases and for every 50 yr between 7000 BC and 1900 AD is shown in Fig. 10.

Not surprisingly the largest rms B_r residuals are observed at high latitudes, particularly in the Southern hemisphere beneath Africa and the Pacific, related to the occurrence of high intensity flux patches. The least difference is observed at mid-latitudes around the northern hemisphere and beneath South America and the SW Pacific where the data distribution is most dense. The low misfit recorded at very high latitudes in the Northern hemisphere is probably a combination of little temporal variability in the reference model due to the rotation around the Earth's axis and the fact that the available data, in particular field intensity, sample the field quite well at the CMB, where we apply our regularization (see fig. 1 of Korte *et al.* 2011).

Comparing the temporal variability of the initial reference field model (for 1840 AD) to the corresponding synthetic model shows that the synthetic model is able to capture both high latitude high intensity flux patches in the northern hemisphere throughout the model time period. For the most part, however, the model only resolves one diffuse high intensity flux patch in the southern hemisphere. This is partially due to the location of the southern hemisphere flux patches in *gufm1* for 1840 AD being situated close to

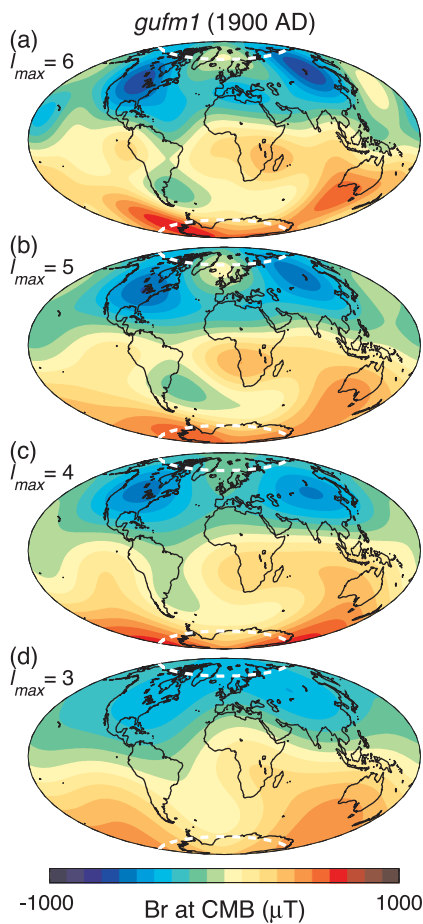


Figure 8. Comparison of the radial component of the field (B_r) at the core mantle boundary (CMB) predicted by *gufm1* truncated at (a) degree $l_{\max} = 6$, (b) degree $l_{\max} = 5$, (c) degree $l_{\max} = 4$ and (d) degree $l_{\max} = 3$. The dashed white lines show the CMB expression ($\sim 71^\circ$ N/S) of the inner core tangent cylinder.

each other. If we change the polarity of the reference model (*gufm1* at 1840 AD) the synthetic model will at times resolve two southern hemisphere flux patches, but usually only when these are located beneath South America and the SW Pacific where there the data distribution is denser (see animation provided in the Supporting Information, Movie 5). This implies that we cannot discriminate between longitudinal drift and growing/weakening flux patches in the southern hemisphere, and even the long-term average persistence of flux patches could be a product of sampling bias.

A similar type of stop-and-go behaviour of the northern hemisphere high latitude flux patches observed in the palaeofield models can be observed in the synthetic models as well, although not to the same degree. This suggests that some of the stop-and-go behaviour could be an effect of the age uncertainties of the data, particularly the correlated uncertainties of the sedimentary data. There is also a tendency of flux patches seemingly appearing, or growing in intensity, as they pass beneath areas with a denser data distribution (as with the southern hemisphere comparison), suggesting that the uneven geographical data distribution could also produce a similar effect.

Fig. 11 shows time-longitude plots of all three new models and the initial synthetic model (*gufm1* at 1840 AD) based on the radial field prediction for the latitude 60° N. In order to emphasize azimuthal structure of the field we also show time-longitude plots after

removing the time-averaged axisymmetric part of the field (Finlay & Jackson 2003). The westward drift of the high latitude flux patches in the northern hemisphere, noted earlier, is visible for the greater part of the last 4000 yr and looks fairly similar to the artificially induced drift of the synthetic model. Interestingly this pattern does not extend further back in time in the palaeofield models, but rather there is a hint of persistent flux patches around -60° and 60° , and possibly also around 180° E, as seen in the long-term time-averaged field (Fig. 6). The presence of the westward drift in the synthetic model throughout the model time period suggests that lack of drift in earlier part in palaeofield models is not due to problems with data distribution and/or uncertainties, but a real feature of the field.

5 CONCLUSIONS

The pfm9k spherical harmonic models represent a new family of low temporal resolution Holocene global geomagnetic field reconstructions. These are intended as alternatives to the widely used CALS10k.1b, covering the same time interval, but also as complements to higher temporal resolution field models covering the last three millennia such as ARCH3k.1, CALS3k.4, A_FM and ASDI_FM.

All three new models show evidence for persistent high latitude high intensity flux at the CMB beneath Greenland, Western Russia, South America and the Pacific Ocean (Fig. 7). However, comparisons with models constrained from synthetic data sets show clear limitations of these predictions for high latitudes in the southern hemisphere. One of the most striking features of the time evolution of the field at the CMB, predicted by all three new models, is a dominant westward motion of northern high latitude high intensity flux patches around the edge of the tangent cylinder during the last 4000 yr. These results are in contrast to similar studies where both westward and eastward drift has been observed to be more or less equally common over the same time period (Dumberry & Finlay 2007; Wardinski & Korte 2008; Amit *et al.* 2011). We find that a combination of the increased weight given to intensity data, which preferentially samples higher latitudes at the CMB (Johnson & McFadden 2007), and the inclusion of high latitude sedimentary declination data (Barletta *et al.* 2008; Lisé-Pronovost *et al.* 2009) are important for tracking the motion of these high latitude flux patches. The new models also show intermittent occurrences of reversed flux at the edge of or inside the tangent cylinder, possibly originating from the equator, but further investigations are required to determine how robust these features are.

The new models are based on essentially the same data as CALS10k.1b but introduce new ways of treating the data, particularly sedimentary data. These include redistributing the weight given to different sources and types of data during the inversion as well as addressing their chronologic uncertainties in a novel way. We find that the single most important change is the resampling of the sedimentary data, effectively reducing the influence of a few individual records that dominated the field reconstructions for some regions of the world, but also reassigning more weight to archaeomagnetic data and data based on more measurements. In future studies, more comprehensive approaches could be used to further distinguish between records based on sedimentation rates and quality estimates such as the scatter of data from different independently oriented cores (Nilsson *et al.* 2010; Panovska *et al.* 2012).

Appropriately treating the sedimentary declination data as relative values has a large impact on the final model outcome, particularly for regions such as the SW Pacific where the models are

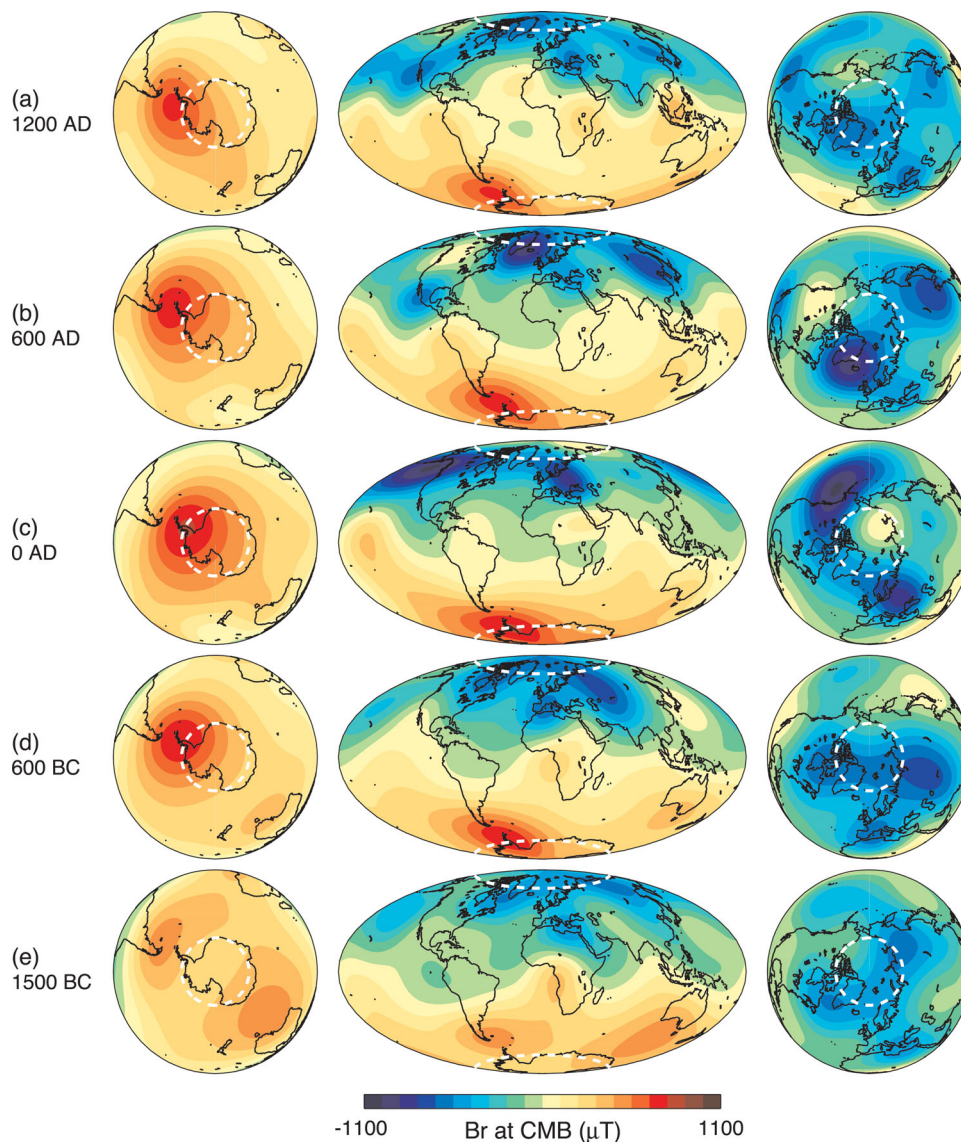


Figure 9. Radial component of the field (B_r) at the core mantle boundary (CMB) of pfm9k.1a at (a) 1200 AD, (b) 600 AD, (c) 0 AD, (d) 600 BC and (e) 1500 BC. Southern hemisphere (left) and northern hemisphere (right) orthographic projections added for clarity. The dashed white lines show the CMB expression ($\sim 71^\circ$ N/S) of the inner core tangent cylinder.

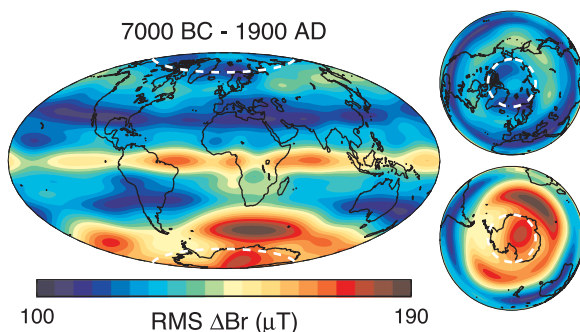


Figure 10. The rms radial field component (B_r) residuals at the core mantle boundary (CMB) between 1000 different reference field models and models constrained by associated synthetic data sets for every 50 yr between 7000 BC and 1900 AD (see text for a more detailed description). The dashed white lines show the CMB expression ($\sim 71^\circ$ N/S) of the inner core tangent cylinder.

dominantly constrained by sedimentary data. As discussed in Section 4.2 the adjustments used here may have led to a slight transfer of power from higher degrees into the dipole component. We conclude that adjustments to the declination data are necessary but that the methodology could be improved. Similar adjustments may also be appropriate for the sedimentary inclination data, which in a few cases appear to be systematically offset by more than 10° based on comparisons with archaeomagnetic data. Like Panovska *et al.* (2012) we did not observe any systematic evidence of inclination shallowing and decided against adjusting the inclination data to avoid removing real persistent non-dipolar features. We note, however, that just by resampling the data most erratic offsets in either (un-adjusted) declination or inclination were successfully identified and removed as outliers by the modelling procedure.

One of the main problems associated with geomagnetic field modelling using sedimentary palaeomagnetic data are the large and often unknown age uncertainties. In the most recent modelling

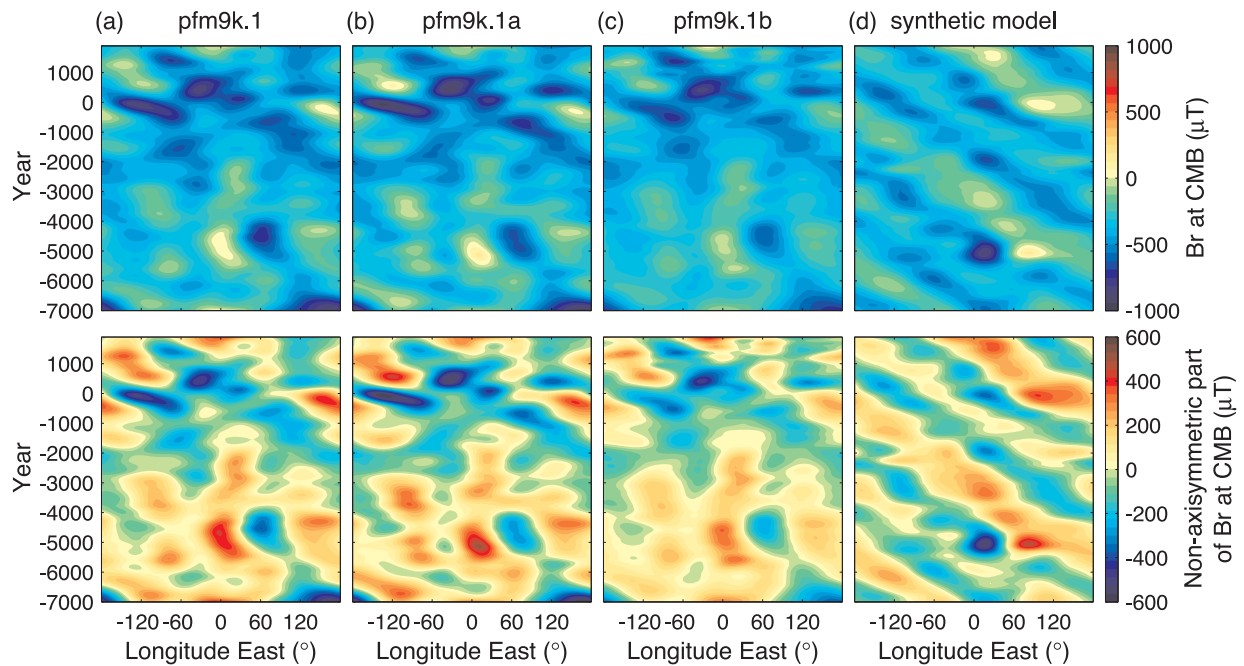


Figure 11. Time Longitude plots of the radial field component (B_r) at the core mantle boundary (CMB) for all three new models and a synthetic model (based on the *gufm1* at 1840 AD, see text for more details) centred around 60°N before (upper panel) and after removal of the time-averaged axisymmetric part of the field (lower panel).

efforts this problem has been approached by bootstrap resampling of the data set, see Section 3.3, whereby one part consists of shifting the whole chronology of each sedimentary record randomly in time by a fixed value of ± 300 yr (Korte *et al.* 2009) or using the smaller published age uncertainties (Licht *et al.* 2013). Here we have instead introduced an alternative, and arguably more realistic, way of adjusting the sediment data chronologies by randomly stretching and compressing the individual timescales of each record. Using this technique we have both been able to assess the likely range of age uncertainties, often up to and most likely also exceeding 500 yr, and adjust the timescale of each record based on comparisons with predictions from pfm9k.1. There are obvious limitations with the methodology applied here, mainly the implicit assumption that the pfm9k.1 is free of chronologic errors. Yet, the results demonstrate the potential information stored in sedimentary data, which can be recovered using the stratigraphic information provided with each record. Temporal smoothing and time-lag related to lock-in processes may also be important but we find that chronologic uncertainties are most likely of greater concern for geomagnetic field reconstructions based on sedimentary data.

The source files for all three models, including the pfm9k.1b individual bootstrap solutions, together with evaluation software are provided in the EarthRef.org Digital Archive (ERDA, <http://www.earthref.org>) by searching for the model names.

ACKNOWLEDGEMENTS

This work was funded by the Natural Environment Research Council, UK, grant numbers NE/I013873/1 and NE/H021043/1. MK acknowledges support from grant KO 2870/4-1 of Deutsche Forschungsgemeinschaft. We thank Catherine Constable and an anonymous reviewer for their constructive reviews of the original manuscript.

REFERENCES

- Ali, M., Oda, H., Hayashida, A., Takemura, K. & Torii, M., 1999. Holocene palaeomagnetic secular variation at Lake Biwa, central Japan, *Geophys. J. Int.*, **136**, 218–228.
- Amit, H., Korte, M., Aubert, J., Constable, C. & Hulot, G., 2011. The time-dependence of intense archeomagnetic flux patches, *J. geophys. Res.: Solid Earth*, **116**, B12106, doi:10.1029/2011JB008538.
- Anson, G.L. & Kodama, K.P., 1987. Compaction-induced inclination shallowing of the post-depositional remanent magnetization in a synthetic sediment, *Geophys. J. R. Astron. Soc.*, **88**, 673–692.
- Barletta, F., St-Onge, G., Channell, J.E.T. & Rochon, A., 2010. Dating of Holocene western Canadian Arctic sediments by matching paleomagnetic secular variation to a geomagnetic field model, *Quat. Sci. Rev.*, **29**, 2315–2324.
- Barletta, F., St-Onge, G., Channell, J.E.T., Rochon, A., Polyak, L. & Darby, D., 2008. High-resolution paleomagnetic secular variation and relative paleointensity records from the western Canadian Arctic: implication for Holocene stratigraphy and geomagnetic field behaviour, *Can. J. Earth Sci.*, **45**, 1265–1281.
- Barton, C.E. & McElhinny, M.W., 1981. A 10 000 yr geomagnetic secular variation record from three Australian maars, *Geophys. J. Int.*, **67**, 465–485.
- Barton, C.E. & Torgersen, T., 1988. Palaeomagnetic and ^{210}Pb estimates of sedimentation in Lake Turkana, East Africa, *Palaeogeogr. Palaeoclimatol. Palaeoecol.*, **68**, 53–60.
- Björck, S. & Wohlfarth, B., 2001. ^{14}C chronostratigraphic techniques in paleolimnology, *Tracking Environmental Change Using Lake Sediments*, pp. 205–245, Kluwer.
- Bleil, U. & Dillon, M., 2008. Holocene Earth's magnetic field variations recorded in marine sediments of the NW African continental margin, *Studia Geophysica et Geodaetica*, **52**, 133–155.
- Blow, R.A. & Hamilton, N., 1978. Effect of compaction on the acquisition of a detrital remanent magnetization in fine-grained sediments, *Geophys. J. R. Astron. Soc.*, **52**, 13–23.
- Bloxham, J., Gubbins, D. & Jackson, A., 1989. Geomagnetic secular variation, *Philos. Trans. R. Soc. Lond. A*, **329**, 415–502.

- Bloxham, J. & Jackson, A., 1992. Time-dependent mapping of the magnetic field at the core-mantle boundary, *J. geophys. Res.: Solid Earth*, **97**, 19 537–19 563.
- Brachfeld, S.A. & Banerjee, S.K., 2000. A new high-resolution geomagnetic relative paleointensity record for the North American Holocene: a comparison of sedimentary and absolute intensity data, *J. geophys. Res.*, **105**, 821–834.
- Brachfeld, S., Acton, G.D., Guyodo, Y. & Banerjee, S.K., 2000. High-resolution paleomagnetic records from Holocene sediments from the Palmer Deep, Western Antarctic Peninsula, *Earth planet. Sci. Lett.*, **181**, 429–441.
- Brown, H., 1981. A palaeomagnetic, geochronological and palaeoenvironmental investigation of late post glacial maar lake sediments from NW Europe, *PhD thesis*, University of Edinburgh, Edinburgh.
- Channell, J.E.T., Hodell, D.A. & Lehman, B., 1997. Relative geomagnetic paleointensity and $\delta^{18}\text{O}$ at ODP Site 983 (Gardar Drift, North Atlantic) since 350 ka, *Earth planet. Sci. Lett.*, **153**, 103–118.
- Chaparro, M.A.E., Böhnell, H.N., Byrne, R., Nowaczyk, N.R., Molinagarza, R.S., Park, J. & Negendank, J.F.W., 2008. Palaeomagnetic secular variation and rock-magnetic studies of Holocene sediments from a maar lake (Hoya de San Nicolas) in Central Mexico, *Geophys. J. Int.*, **175**, 462–476.
- Constable, C.G., 1985. Eastern Australian geomagnetic field intensity over the past 14000 yr, *Geophys. J. R. Astron. Soc.*, **81**, 121–130.
- Constable, C.G. & McElhinny, M.W., 1985. Holocene geomagnetic secular variation records from north-eastern Australian lake sediments, *Geophys. J. Int.*, **81**, 103–120.
- Constable, C.G., Johnson, C.L. & Lund, S.P., 2000. Global geomagnetic field models for the past 3000 years: transient or permanent flux lobes?, *Philos. Trans. R. Soc. Lond. A*, **358**, 991–1008.
- Creer, K.M., Readman, P.W. & Papamarinopoulos, S., 1981. Geomagnetic secular variations in Greece through the last 6000 years obtained from lake sediment studies, *Geophys. J. Int.*, **66**, 193–219.
- Creer, K.M., Valencio, D.A., Sinito, A.M., Tucholka, P. & Vilas, J.F.A., 1983. Geomagnetic secular variations 0–14 000 yr BP as recorded by lake sediments from Argentina, *Geophys. J. R. Astron. Soc.*, **74**, 199–221.
- Donadini, F., Korhonen, K., Riisager, P. & Pesonen, L.J., 2006. Database for Holocene geomagnetic intensity information, *EOS, Trans. Am. geophys. Un.*, **87**, 137–138.
- Donadini, F., Korte, M. & Constable, C.G., 2009. Geomagnetic field for 0–3 ka: 1. New data sets for global modeling, *Geochem. Geophys. Geosyst.*, **10**, Q06007, doi:10.1029/2008GC002295.
- Doner, L., 2003. Late-Holocene paleoenvironments of northwest Iceland from lake sediments, *Palaeogeogr. Palaeoclimatol. Palaeoecol.*, **193**, 535–560.
- Dumberry, M. & Bloxham, J., 2006. Azimuthal flows in the Earth's core and changes in length of day at millennial timescales, *Geophys. J. Int.*, **165**, 32–46.
- Dumberry, M. & Finlay, C.C., 2007. Eastward and westward drift of the Earth's magnetic field for the last three millennia, *Earth planet. Sci. Lett.*, **254**, 146–157.
- Finlay, C.C. & Jackson, A., 2003. Equatorially dominated magnetic field change at the surface of Earth's core, *Science*, **300**, 2084–2086.
- Fisher, R., 1953. Dispersion on a sphere, *Proc. R. Soc. Lond. Ser. A*, **217**, 295–305.
- Frank, U., 2007. Palaeomagnetic investigations on lake sediments from NE China: a new record of geomagnetic secular variations for the last 37 ka, *Geophys. J. Int.*, **169**, 29–40.
- Frank, U., Nowaczyk, N.R., Negendank, J.F.W. & Melles, M., 2002a. A paleomagnetic record from Lake Lama, northern Central Siberia, *Phys. Earth planet. Inter.*, **133**, 3–20.
- Frank, U., Schwab, M.J. & Negendank, J.F.W., 2002b. A lacustrine record of paleomagnetic secular variations from Birkat Ram, Golan Heights (Israel) for the last 4400 years, *Phys. Earth planet. Inter.*, **133**, 21–34.
- Frank, U., Schwab, M.J. & Negendank, J.F.W., 2003. Results of rock magnetic investigations and relative paleointensity determinations on lacustrine sediments from Birkat Ram, Golan Heights (Israel), *J. geophys. Res.: Solid Earth*, **108**, 2379, doi:10.1029/2002JB002049.
- Frank, U., Nowaczyk, N.R. & Negendank, J.F.W., 2007. Palaeomagnetism of greigite bearing sediments from the Dead Sea, Israel, *Geophys. J. Int.*, **168**, 904–920.
- Gallet, Y., Hulot, G., Chulliat, A. & Genevey, A., 2009. Geomagnetic field hemispheric asymmetry and archeomagnetic jerks, *Earth planet. Sci. Lett.*, **284**, 179–186.
- Geiss, C.E., Dorale, J.A. & Dahms, D., 2007. A rockmagnetic and palaeomagnetic record of two glacial lakes in the Wind River Range, Wyoming, USA, *EOS, Trans. Am. geophys. Un.*, Abstract GP53B-1216.
- Genevey, A., Gallet, Y., Constable, C.G., Korte, M. & Hulot, G., 2008. ArcheoInt: an upgraded compilation of geomagnetic field intensity data for the past ten millennia and its application to the recovery of the past dipole moment, *Geochem. Geophys. Geosyst.*, **9**, Q04038, doi:10.1029/2007GC001881.
- Gogorza, C.S.G., Sinito, A.M., Lirio, J.M., Nuñez, H., Chaparro, M. & Vilas, J.F., 2002. Paleosecular variations 0–19,000 years recorded by sediments from Escondido Lake (Argentina), *Phys. Earth planet. Inter.*, **133**, 35–55.
- Gogorza, C.S.G., Lirio, J.M., Nuñez, H., Chaparro, M., Bertorello, H.R. & Sinito, A.M., 2004. Paleointensity studies on Holocene-Pleistocene sediments from lake Escondido, Argentina, *Phys. Earth Planet. Inter.*, **145**, 219–238.
- Gogorza, C.S.G., Irurzun, M.A., Chaparro, M.A.E., Lirio, J.M., Nuñez, H., Bercoff, P.G. & Sinito, A.M., 2006. Relative paleointensity of the geomagnetic field over the last 21,000 years BP from sediment cores, Lake El Trébol (Patagonia, Argentina), *Earth Planets Space*, **58**, 1323–1332.
- Gubbins, D., 1975. Can the Earth's magnetic field be sustained by core oscillations?, *Geophys. Res. Lett.*, **2**, 409–412.
- Hagstrum, J.T. & Champion, D.E., 2002. A Holocene paleosecular variation record from ^{14}C -dated volcanic rocks in western North America, *J. geophys. Res.*, **107**, 2025, doi:10.1029/2001JB000524.
- Haltia-Hovi, E., Nowaczyk, N. & Saarinen, T., 2010. Holocene palaeomagnetic secular variation recorded in multiple lake sediment cores from eastern Finland, *Geophys. J. Int.*, **180**, 609–622.
- Hayashida, A., Ali, M., Kuniko, Y., Kitagawa, H., Torii, M. & Takemura, K., 2007. Environmental magnetic record and paleosecular variation data for the last 40 kyrs from the Lake Biwa sediments, Central Japan, *Earth Planets Space*, **59**, 807–814.
- Hillenbrand, C.-D. et al., 2010. Age assignment of a diatomaceous ooze deposited in the western Amundsen Sea Embayment after the Last Glacial Maximum, *J. Quat. Sci.*, **25**, 280–295.
- Hogg, E., 1978. The Holocene geomagnetic field in Europe, *PhD thesis*, University of Edinburgh, Edinburgh, U.K.
- Hongre, L., Hulot, G. & Khokhlov, A., 1998. An analysis of the geomagnetic field over the past 2000 years, *Phys. Earth planet. Inter.*, **106**, 311–335.
- Huttunen, P. & Stober, J., 1980. Dating of palaeomagnetic records from Finnish lake sediment cores using pollen analysis, *Boreas*, **9**, 193–202.
- Hyodo, M. et al., 1999. A Late Holocene geomagnetic secular variation record from Erhai Lake, southwest China, *Geophys. J. Int.*, **136**, 784–790.
- Irurzun, M.A., Gogorza, C.S.G., Chaparro, M.A.E., Lirio, J.M., Nunez, H., Vilas, J.F. & Sinito, A.M., 2006. Paleosecular variations recorded by Holocene-Pleistocene sediments from Lake El Trébol (Patagonia, Argentina), *Phys. Earth planet. Inter.*, **154**, 1–17.
- Jackson, A., Jonkers, A.R.T. & Walker, M.R., 2000. Four centuries of geomagnetic secular variation from historical records, *Philos. Trans. R. Soc. Lond., A*, **358**, 957–990.
- Johnson, C.L. & McFadden, P.L., 2007. Time-averaged field and paleosecular variation. In *Treatise on Geophysics: Geomagnetism*, vol. 5, pp. 417–453, ed. Kono, M., Elsevier.
- King, J.W., 1983. Geomagnetic secular variation curves for northeastern North America for the last 9000 years, *PhD thesis*, University of Minnesota, Minneapolis.
- Knudsen, M.F., Riisager, P., Donadini, F., Snowball, I., Muscheler, R., Korhonen, K. & Pesonen, L.J., 2008. Variations in the geomagnetic dipole moment during the Holocene and the past 50 kyr, *Earth planet. Sci. Lett.*, **272**, 319–329.

- Korhonen, K., Donadini, F., Riisager, P. & Pesonen, L.J., 2008. GEOMA-GIA50: an archeointensity database with PHP and MySQL, *Geochem. Geophys. Geosyst.*, **9**, Q04029, doi:10.1029/2007GC001893.
- Korte, M. & Constable, C.G., 2003. Continuous global geomagnetic field models for the past 3000 years, *Phys. Earth planet. Inter.*, **140**, 73–89.
- Korte, M. & Constable, C.G., 2005. Continuous geomagnetic field models for the past 7 millennia: 2. CALS7K, *Geochem. Geophys. Geosyst.*, **6**, Q02H16, doi:10.1029/2004GC000801.
- Korte, M. & Constable, C.G., 2006. On the use of calibrated relative paleointensity records to improve millennial-scale geomagnetic field models, *Geochem. Geophys. Geosyst.*, **7**, Q09004, doi:10.1029/2006GC001368.
- Korte, M. & Constable, C.G., 2011. Improving geomagnetic field reconstructions for 0–3 ka, *Phys. Earth planet. Inter.*, **188**, 247–259.
- Korte, M. & Holme, R., 2010. On the persistence of geomagnetic flux lobes in global Holocene field models, *Phys. Earth planet. Inter.*, **182**, 179–186.
- Korte, M., Genevey, A., Constable, C.G., Frank, U. & Schnepf, E., 2005. Continuous geomagnetic field models for the past 7 millennia: 1. A new global data compilation, *Geochem. Geophys. Geosyst.*, **6**, Q02H15, doi:10.1029/2004GC000800.
- Korte, M., Donadini, F. & Constable, C.G., 2009. Geomagnetic field for 0–3 ka: 2. A new series of time-varying global models, *Geochem. Geophys. Geosyst.*, **10**, Q06008, doi:10.1029/2008GC002297.
- Korte, M., Constable, C., Donadini, F. & Holme, R., 2011. Reconstructing the Holocene geomagnetic field, *Earth planet. Sci. Lett.*, **312**, 497–505.
- Lal, D., 1988. Theoretically expected variations in the terrestrial cosmic-ray production rates of isotopes. in *Solar-Terrestrial Relationships and the Earth Environment in the last Millennia*, pp. 216–233, ed. Castagnoli, G.C., North-Holland Publishing Company.
- Lal, D. & Peters, B., 1967. Cosmic ray produced radioactivity on the earth, in *Handbuch der Physik Band XLVI/2*, pp. 551–612, Springer-Verlag.
- Licht, A., Hulot, G., Gallet, Y. & Thébault, E., 2013. Ensembles of low degree archeomagnetic field models for the past three millennia, *Phys. Earth planet. Inter.*, **224**, 38–67.
- Lifton, N., Smart, D.F. & Shea, M.A., 2008. Scaling time-integrated in situ cosmogenic nuclide production rates using a continuous geomagnetic model, *Earth planet. Sci. Lett.*, **268**, 190–201.
- Lisé-Pronovost, A., St-Onge, G., Brachfeld, S., Barletta, F. & Darby, D., 2009. Paleomagnetic constraints on the Holocene stratigraphy of the Arctic Alaskan margin, *Global Planet. Change*, **68**, 85–99.
- Lodge, A. & Holme, R., 2009. Towards a new approach to archaeomagnetic dating in Europe using geomagnetic field modelling, *Archaeometry*, **51**, 309–322.
- Lund, S.P. & Banerjee, S.K., 1985. Late quaternary paleomagnetic field secular variation from two Minnesota Lakes, *J. geophys. Res.*, **90**, 803–825.
- Mothersill, J.S., 1979. The palaeomagnetic record of the late Quaternary sediments of Thunder Bay, *Can. J. Earth Sci.*, **16**, 1016–1023.
- Mothersill, J.S., 1981. Late Quaternary palaeomagnetic record of the Goderich Basin, lake Huron, *Can. J. Earth Sci.*, **18**, 448–456.
- Mothersill, J., 1996. Paleomagnetic results from lakes Victoria and Albert, Uganda, *Studia Geophysica et Geodaetica*, **40**, 25–35.
- Muscheler, R., Beer, J., Wagner, G., Laj, C., Kissel, C., Raisbeck, G.M., You, F. & Kubik, P.W., 2004. Changes in the carbon cycle during the last deglaciation as indicated by the comparison of ^{10}Be and ^{14}C records, *Earth planet. Sci. Lett.*, **219**, 325–340.
- Muscheler, R., Beer, J., Kubik, P.W. & Synal, H.A., 2005. Geomagnetic field intensity during the last 60,000 years based on ^{10}Be and ^{36}Cl from the Summit ice cores and ^{14}C , *Quat. Sci. Rev.*, **24**, 1849–1860.
- Muscheler, R., Joos, F., Beer, J., Müller, S.A., Vonmoos, M. & Snowball, I., 2007. Solar activity during the last 1000 yr inferred from radionuclide records, *Quat. Sci. Rev.*, **26**, 82–97.
- Nilsson, A., Snowball, I., Muscheler, R. & Uvo, C.B., 2010. Holocene geocentric dipole tilt model constrained by sedimentary paleomagnetic data, *Geochem. Geophys. Geosyst.*, **11**, Q08018, doi:10.1029/2010GC003118.
- Nilsson, A., Muscheler, R. & Snowball, I., 2011. Millennial scale cyclicity in the geodynamo inferred from a dipole tilt reconstruction, *Earth planet. Sci. Lett.*, **311**, 299–305.
- Nurgaliev, D.K., Boisson, A.S., Heller, F., Burov, B.V., Jasonov, P.G., Khasanov, D.I. & Ibragimov, S.Z., 1996. Geomagnetic secular variation through the last 3500 years as recorded by lake Aslikul sediments from eastern Europe (Russia), *Geophys. Res. Lett.*, **23**, 375–378.
- Nourgaliev, D.K., Heller, F., Borisov, A.S., Hajdas, I., Bonani, G., Iassonov, P.G. & Oberhänsli, H., 2003. Very high resolution paleosecular variation record for the last ~1200 years from the Aral Sea, *Geophys. Res. Lett.*, **30**, doi:10.1029/2003GL018145.
- Nourgaliev, D.K., Heller, F., Borisov, A.C., Yasanov, P.G., Chernova, I.Y. & Hajdas, I., 2005. Principal features (master curve) of geomagnetic field variations in Belorussia during the last 12 thousand years, *Russ. J. Earth Sci.*, **7**, 1–16.
- Ojala, A.E.K. & Saarinen, T., 2002. Palaeosecular variation of the Earth's magnetic field during the last 10000 years based on the annually laminated sediment of Lake Nautajärvi, central Finland, *Holocene*, **12**, 391–400.
- Ojala, A.E.K. & Tiljander, M., 2003. Testing the fidelity of sediment chronology: comparison of varve and paleomagnetic results from Holocene lake sediments from central Finland, *Quat. Sci. Rev.*, **22**, 1787–1803.
- Olson, P. & Deguen, R., 2012. Eccentricity of the geomagnetic dipole caused by lopsided inner core growth, *Nature Geosci.*, **5**, 565–569.
- Panovska, S., Finlay, C.C., Donadini, F. & Hirt, A.M., 2012. Spline analysis of Holocene sediment magnetic records: uncertainty estimates for field modeling, *J. geophys. Res.*, **117**, B02101, doi:10.1029/2011JB008813.
- Pavón-Carrasco, F.J., Osete, M.L., Torta, J.M. & Gaya-Piqué, L.R., 2009. A regional archeomagnetic model for Europe for the last 3000 years, SCHA.DIF.3K: applications to archeomagnetic dating, *Geochem. Geophys. Geosyst.*, **10**, Q03013, doi:10.1029/2008GC002244.
- Peck, J.A., King, J.W., Colman, S.M. & Kravchinsky, V.A., 1996. An 84-kyr paleomagnetic record from the sediments of Lake Baikal, Siberia, *J. geophys. Res.*, **101**, 11 365–11 386.
- Peng, L. & King, J.W., 1992. A late Quaternary geomagnetic secular variation record from Lake Waiau, Hawaii, and the question of the Pacific Nondipole low, *J. geophys. Res.*, **97**, 4407–4424.
- Richter, C., Venuti, A., Verosub, K.L. & Wei, K.-Y., 2006. Variations of the geomagnetic field during the Holocene: relative paleointensity and inclination record from the West Pacific (ODP Hole 1202B), *Phys. Earth planet. Inter.*, **156**, 179–193.
- Roberts, A.P. & Winkhofer, M., 2004. Why are geomagnetic excursions not always recorded in sediments? Constraints from post-depositional remanent magnetization lock-in modelling, *Earth planet. Sci. Lett.*, **227**, 345–359.
- Saarinen, T., 1998. High-resolution palaeosecular variation in northern Europe during the last 3200 years, *Phys. Earth planet. Inter.*, **106**, 299–309.
- Skilling, J., 2006. Nested sampling for general Bayesian computation, *Bayesian Anal.*, **1**, 833–860.
- Snowball, I. & Muscheler, R., 2007. Palaeomagnetic intensity data: an Achilles heel of solar activity reconstructions, *Holocene*, **17**, 851–859.
- Snowball, I. & Sandgren, P., 2002. Geomagnetic field variations in northern Sweden during the Holocene quantified from varved lake sediments and their implications for cosmogenic nuclide production rates, *Holocene*, **12**, 517–530.
- Snowball, I. & Sandgren, P., 2004. Geomagnetic field intensity changes in Sweden between 9000 and 450 cal BP: extending the record of “archaeomagnetic jerks” by means of lake sediments and the pseudo-Thellier technique, *Earth planet. Sci. Lett.*, **227**, 361–376.
- Snowball, I., Zillen, L., Ojala, A., Saarinen, T. & Sandgren, P., 2007. Fennoscandian and Fennoripis: Varve dated Holocene palaeomagnetic secular variation and relative paleointensity stacks for Fennoscandia, *Earth planet. Sci. Lett.*, **255**, 106–116.
- St-Onge, G., Stoner, J.S. & Hillaire-Marcel, C., 2003. Holocene paleomagnetic records from the St. Lawrence Estuary, eastern Canada: centennial-to millennial-scale geomagnetic modulation of cosmogenic isotopes, *Earth planet. Sci. Lett.*, **209**, 113–130.
- St-Onge, G., Mulder, T., Piper, D.J.W., Hillaire-Marcel, C. & Stoner, J.S., 2004. Earthquake and flood-induced turbidites in the Saguenay Fjord

- (Québec): a Holocene paleoseismicity record, *Quat. Sci. Rev.*, **23**, 283–294.
- Stockhausen, H., 1998. Geomagnetic palaeosecular variation (0–13 000 yr BP) as recorded in sediments from three maar lakes from the West Eifel (Germany), *Geophys. J. Int.*, **135**, 898–910.
- Stoner, J.S., Jennings, A., Kristjánsson, G.B., Dunhill, G., Andrews, J.T. & Hardardóttir, J., 2007. A paleomagnetic approach toward refining Holocene radiocarbon-based chronologies: paleoceanographic records from the north Iceland (MD99–2269) and east Greenland (MD99–2322) margins, *Paleoceanography*, **22**, PA1209, doi:10.1029/2006PA001285.
- Suttie, N., Holme, R., Hill, M.J. & Shaw, J., 2011. Consistent treatment of errors in archaeointensity implies rapid decay of the dipole prior to 1840, *Earth planet. Sci. Lett.*, **304**, 13–21.
- Tauxe, L., 2005. Inclination flattening and the geocentric axial dipole hypothesis, *Earth planet. Sci. Lett.*, **233**, 247–261.
- Thompson, R. & Turner, G.M., 1985. Icelandic Holocene palaeolimnomagnetism, *Phys. Earth planet. Inter.*, **38**, 250–261.
- Thouveny, N. & Williamson, D., 1988. Palaeomagnetic study of the Holocene and Upper Pleistocene sediments from Lake Barombi Mbo, Cameroun: first results, *Phys. Earth planet. Inter.*, **52**, 193–206.
- Turner, G.M., 1987. A 5000 year geomagnetic palaeosecular variation record from western Canada, *Geophys. J. R. Astron. Soc.*, **91**, 103–121.
- Turner, G.M. & Lillis, D.A., 1994. A palaeomagnetic secular variation record for New Zealand during the past 2500 years, *Phys. Earth planet. Inter.*, **83**, 265–282.
- Turner, G.M. & Thompson, R., 1979. Behaviour of the earth's magnetic field as recorded in the sediment of Loch Lomond, *Earth planet. Sci. Lett.*, **42**, 412–426.
- Turner, G.M. & Thompson, R., 1981. Lake sediment record of the geomagnetic secular variation in Britain during Holocene times, *Geophys. J. Int.*, **65**, 703–725.
- Valet, J.-P., Herrero-Bervera, E., Le Mouél, J.-L. & Plenier, G., 2008. Secular variation of the geomagnetic dipole during the past 2000 years, *Geochem. Geophys. Geosyst.*, **9**, Q01008, doi:10.1029/2007GC001728.
- Verosub, K.L., Mehringer, P.J. & Waterstraat, P., 1986. Holocene secular variation in Western North America: paleomagnetic record from Fish Lake, Harney County, Oregon, *J. geophys. Res.*, **91**, 3609–3623.
- Vigliotti, L., 2006. Secular variation record of the Earth's magnetic field in Italy during the Holocene: constraints for the construction of a master curve, *Geophys. J. Int.*, **165**, 414–429.
- Vonmoos, M., Beer, J. & Muscheler, R., 2006. Large variations in Holocene solar activity: constraints from ^{10}Be in the Greenland Ice Core Project ice core, *J. geophys. Res.*, **111**, A10105, doi:10.1029/2005JA011500.
- Wardinski, I. & Korte, M., 2008. The evolution of the core-surface flow over the last seven thousands years, *J. geophys. Res.: Solid Earth*, **113**, B05101, doi:10.1029/2007JB005024.
- Weeks, R., Laj, C., Endignoux, L., Fuller, M., Roberts, A., Manganne, R., Blanchard, E. & Goree, W., 1993. Improvements in long-core measurement techniques: applications in palaeomagnetism and palaeoceanography, *Geophys. J. Int.*, **114**, 651–662.

- Yang, X., Heller, F., Yang, J. & Su, Z., 2009. Paleosecular variations since ~9000 yr BP as recorded by sediments from maar lake Shuangchiling, Hainan, South China, *Earth planet. Sci. Lett.*, **288**, 1–9.
- Zillén, I., 2003. Setting the Holocene clock using varved lake sediments in Sweden, *LUNDQUA PhD thesis*, Lund University, Lund.

SUPPORTING INFORMATION

Additional Supporting Information may be found in the online version of this article:

Movie 1. Radial component of the field (Br) at the core mantle boundary (CMB) predicted by pfm9k.1 between 7000 BC and 1900 AD. The white lines show the CMB expression ($\sim 71^\circ$ N/S) of the inner core tangent cylinder.

Movie 2. Radial component of the field (Br) at the core mantle boundary (CMB) predicted by pfm9k.1a between 7000 BC and 1900 AD. The white lines show the CMB expression ($\sim 71^\circ$ N/S) of the inner core tangent cylinder.

Movie 3. Radial component of the field (Br) at the core mantle boundary (CMB) predicted by pfm9k.1b between 7000 BC and 1900 AD. The white lines show the CMB expression ($\sim 71^\circ$ N/S) of the inner core tangent cylinder.

Movie 4. Radial component of the field (Br) at the core mantle boundary (CMB) of a reference field model (Upper panel) and a synthetic model (Lower panel) based on data resampled from the reference field (see text for more information). The reference field model is based on the gufm1 prediction at 1840 AD extended backwards and forwards in time with a continuous westward rotation. The white lines show the CMB expression ($\sim 71^\circ$ N/S) of the inner core tangent cylinder.

Movie 5. Radial component of the field (Br) at the core mantle boundary (CMB) of a reference field model (Upper panel) and a synthetic model (Lower panel) based on data resampled from the reference field (see text for more information). The reference field model is based on the gufm1 prediction at 1840 AD with reversed polarity and extended backwards and forwards in time with a continuous westward rotation. The white lines show the CMB expression ($\sim 171^\circ$ N/S) of the inner core tangent cylinder (<http://gji.oxfordjournals.org/lookup/suppl/doi:10.1093/gji/ggu120/-/DC1>)

Please note: Oxford University Press is not responsible for the content or functionality of any supporting materials supplied by the authors. Any queries (other than missing material) should be directed to the corresponding author for the article.